

---

# Binary Radiance Fields

---

**Seungjoo Shin**  
GSAI, POSTECH  
seungjoo.shin@postech.ac.kr

**Jaesik Park**  
CSE & IPAI, Seoul National University  
jaesik.park@snu.ac.kr

## Abstract

In this paper, we propose *binary radiance fields* (BiRF), a storage-efficient radiance field representation employing binary feature encoding that encodes local features using binary encoding parameters in a format of either  $+1$  or  $-1$ . This binarization strategy lets us represent the feature grid with highly compact feature encoding and a dramatic reduction in storage size. Furthermore, our 2D-3D hybrid feature grid design enhances the compactness of feature encoding as the 3D grid includes main components while 2D grids capture details. In our experiments, binary radiance field representation successfully outperforms the reconstruction performance of state-of-the-art (SOTA) efficient radiance field models with lower storage allocation. In particular, our model achieves impressive results in static scene reconstruction, with a PSNR of 32.03 dB for Synthetic-NeRF scenes, 34.48 dB for Synthetic-NSVF scenes, 28.20 dB for Tanks and Temples scenes while only utilizing 0.5 MB of storage space, respectively. We hope the proposed binary radiance field representation will make radiance fields more accessible without a storage bottleneck.

## 1 Introduction

In recent years, the emergence of Neural Radiance Fields (NeRF) [1] has greatly impacted 3D scene modeling and novel-view synthesis. The methodology models a complex volumetric scene as an implicit function that maps positional and directional information of sampled points to the corresponding color and density values, enabling the rendering of photo-realistic novel views from any desired viewpoints. Subsequent advancements [2, 3, 4, 5, 6, 7, 8, 9, 10] have demonstrated their ability to reconstruct various 3D scenes using images and corresponding camera poses, which opens radiance fields as a promising approach for representing the real 3D world.

Despite the significant progress, the computational burden of large-scale multi-layer perceptrons (MLPs) remains a critical challenge, leading to a speed issue in both training and rendering radiance fields. To tackle this issue, an auxiliary explicit voxel grid has been utilized for encoding local features, denoting a voxel-based method. While the implicit radiance field representations must compute and update all learnable parameters in MLPs, parametric encoding calculates only a small portion of encoded features leading to less computational cost. The voxel-based feature encoding has been implemented in various data structures, such as dense grids [11, 12], octrees [13, 14], sparse voxel grids [15], decomposed grids [16, 17, 18, 19], and hash tables [20]. These representations succeed in efficiently reducing the time required for convergence and inference. Nonetheless, explicit feature encoding methods have a significant disadvantage: their excessive storage usage. Now, we are facing a new bottleneck that restricts accessibility. Consequently, the desire for a new radiance field representation to implement a realistic 3D scene with little storage has been raised.

This paper introduces a new binary feature encoding to represent storage-efficient radiance fields with binary feature grids, referred to as *binary radiance fields* (BiRF). Here, we focus on embedding sufficient feature information restricted in binary format. We achieve this by adopting a binarization-aware training scheme, binary feature encoding, that constraints feature encoding parameters to either

+1 or  $-1$  and update them during optimization, inspired by Binarized Neural Networks (BNNs) [21]. Accordingly, our radiance field representation can successfully reconstruct complicated 3D scenes with binary encoding parameters that can be represented using compact data resulting in a storage-efficient radiance field model. Furthermore, we extend the modern multi-resolution hash encoding architecture to a 3D voxel grid and three orthogonal 2D plane grids. This hybrid structure allows for more efficient feature capture in a more compact manner.

As a result, our radiance field model achieves superior reconstruction performance compared to prior efficient and lightweight methods. To be specific, our model attains outstanding performance in static scene reconstruction, with a PSNR of 32.03 dB for Synthetic-NeRF scenes, 34.48 dB for Synthetic-NSVF scenes, 28.20 dB for Tanks and Temples scenes while only utilizing 0.5 MB of storage space, respectively.

We summarize our contributions as follows:

- We propose *binary radiance fields* (BiRF), a binary radiance field representation that concisely encodes the binary feature values of either  $+1$  or  $-1$  in 2D-3D hybrid feature grid to represent storage-efficient radiance fields.
- Our binarization-aware training scheme, binary feature encoding, allows us to effectively encode the feature information with binary parameters and update these parameters during optimization.
- We demonstrate that our representation achieves superior performance despite requiring only minimal storage space, even in 0.5 MB for Synthetic-NeRF scenes.

## 2 Related Work

**Neural Radiance Fields** Neural radiance fields (NeRF) [1] is a leading method for novel-view synthesis by reconstructing high-quality 3D scenes. To achieve scene representation, it optimizes coordinate-based multi-layer perceptrons (MLPs) to estimate the color and density values of the 3D scene via differentiable volume rendering.

Improving radiance field representations begins with embracing diverse scenarios where the scene is intricate. The sampling strategy used in the original NeRF assumes that the entire scene can fit within a bounded volume, which limits its ability to capture background elements in an unbounded scene. To address this issue, several works [2, 3] have separately modeled foreground and background by re-parameterizing the 3D space. These parameterizations have been primarily applied in unbounded  $360^\circ$  view captured scenes. Additionally, due to insufficient capacity, NeRF’s lighting components have limitations in dealing with glossy surfaces. To address this challenge, transmitted and reflected radiance are optimized separately [4, 5]. Furthermore, there are approaches to extend to a dynamic domain with object movements [6, 7, 8, 22, 23].

Despite performing impressive results, it has limitations, including slow training and rendering speed. It relies solely on utilizing implicit functions for 3D scene representation, which may lead to computational inefficiencies [20].

**Radiance Fields Representations** NeRF methods can be categorized into three types: implicit [1, 2, 3, 24, 25, 26, 27], explicit [14, 15, 18, 28], and hybrid representations [11, 12, 13, 17, 20, 23, 29, 30, 31], depending on how the approach represent the scenes.

Implicit representations extensively use neural networks to represent radiance fields, as done in the pioneering method [1]. The network has a simple structure and can render photo-realistic images with few parameters. However, they take a lot of time to converge and require significant inference time because they share the entire weight and bias parameters of the MLPs for an arbitrary input coordinate, resulting in a significant computational cost. Therefore, recent studies have proposed explicit and hybrid radiance field representations to overcome the slow speed by incorporating explicit data structures (such as 2D/3D grids or 3D points) for local feature encoding.

Explicit representations directly encode view-dependent color and opacity values with basis functions (e.g., spherical harmonics). For instance, PlenOctrees [14] bakes implicit radiance fields into an octree structure for rendering speed acceleration. Plenoxels [15] uses a sparse voxel structure, and the approach by Zhang et al. [28] utilize a point cloud. Similarly, CCNeRF [18] employs low-rank tensor grids for 3D scene manipulation. On the other hand, hybrid representations utilize encoded local

features as input for the MLPs. NSVF [13] achieves fast rendering speed thanks to the octree structure. To store local features, Point-NeRF [29] uses a point cloud, DVGO [11, 12] employs two dense voxel grids, and TensoRF [17] makes use of a factorized tensor grid. More recently, Instant-NGP [20] introduces a multi-resolution hash encoding technique that has demonstrated exceptional effectiveness in terms of convergence and rendering speed, achieving superior performance. Additionally, Zhan et al. [32] introduce a learning method of the gauge transformation in radiance fields.

While explicit and hybrid representations boost training time and rendering speed, they inevitably suffer from the critical disadvantage of large storage consumption due to excessive local features. In this study, we construct a multi-resolution 2D-3D hybrid grid by combining 2D planes and 3D grids and binarizing their encoding parameters to fully leverage their minimal information of them.

**Radiance Fields Compression** Despite the acceleration of training and rendering, the explicit and the hybrid radiance fields have difficulties utilized in various applications due to their large storage. Consequently, there are several attempts to reduce the storage of the models.

For instance, PlenOctrees [14] and Plenoxels [15] filter the voxels using weight-based thresholding for leaving only the set of sparse voxels, which are sufficient to represent the scene. The distortion loss in DVGO-v2 [12] enables it to achieve better quality and greater resolution compactness. Other approaches apply bit quantization after the training. PlenOctrees [14], PerFception [33], and Re:NeRF [34] all apply low-bit quantization of trained local features. VQAD [35] compresses the feature grid parameters into a small codebook with learned indices. Re:NeRF [34] and VQRF [36] have proposed methods for compressing existing explicit or hybrid radiance field models, including post-optimization processes. Also, Rho et al. [37] achieve high storage efficiency by applying wavelet transform on hybrid radiance field models with learnable masks.

Although the post-processing approaches above successfully reduce the storage requirements of the radiance field models, they have several disadvantages. Firstly, they require additional optimization steps for compression, which can be time-consuming. Also, their performance is bounded by the performance of the pre-trained models. In contrast, our approach performs binarization during training with the efficient 2D/3D feature grid representation. Our approach does not require any post-optimization processes and shows better rendering quality with even smaller storage space.

### 3 Preliminaries

The methodology of NeRF [1] optimizes a 5D function, as a radiance field representation, to model a continuous volumetric scene with a view-dependent effect. The implicit 5D function, which consists of MLPs, maps a 3D coordinate  $\mathbf{x} \in (x, y, z)$  and a 2D viewing direction  $\mathbf{d} = (\theta, \phi)$  to an emitted color  $\mathbf{c} = (r, g, b)$  and a volume density  $\sigma$ :

$$(\mathbf{c}, \sigma) = \text{MLP}_{\Theta}(\mathbf{x}, \mathbf{d}). \quad (1)$$

Due to the use of an implicit function, updating all the weight and bias parameters of MLPs is necessary to train a single point. Consequently, this leads to slow convergence, requiring more than a day to optimize a scene.

For volume rendering, the colors  $\{\mathbf{c}_i\}$  and densities  $\{\sigma_i\}$  of sampled points along a ray  $\mathbf{r}(t) = \mathbf{o} + t\mathbf{d}$  are accumulated to obtain the color of the ray:

$$\hat{\mathbf{C}}(\mathbf{r}) = \sum_N^{i=1} T_i \alpha_i \mathbf{c}_i, \quad T_i = \prod_{j=1}^{i-1} (1 - \alpha_j), \quad \alpha_i = 1 - \exp(-\sigma_i \delta_i), \quad (2)$$

where  $T_i$  and  $\alpha_i$  represent accumulated transmittance and alpha of  $i$ -th sampled point, respectively.  $\delta_i = t_{i+1} - t_i$  denotes the distance between adjacent points. Recently, an occupancy grid [20] is adopted to skip non-empty space for efficient ray sampling, leading to an advance in rendering speed.

To accelerate the rendering process, the hybrid representations [11, 17, 20] have been developed to encode local features in explicit data structures  $\Phi_{\theta}$  (e.g., 2D/3D grid). These features are then linearly interpolated and used as inputs for small MLPs to predict colors and densities:

$$\mathbf{f} = \text{interp}(\mathbf{x}, \Phi_{\theta}), \quad (\mathbf{c}, \sigma) = \text{MLP}_{\Theta}(\mathbf{f}, \mathbf{d}), \quad (3)$$

where  $\text{interp}$  means a linear interpolation operator, and  $\mathbf{f}$  denotes a interpolated feature. The choice of explicit data structure  $\Phi_{\theta}$  significantly affects the number of learnable parameters and hence

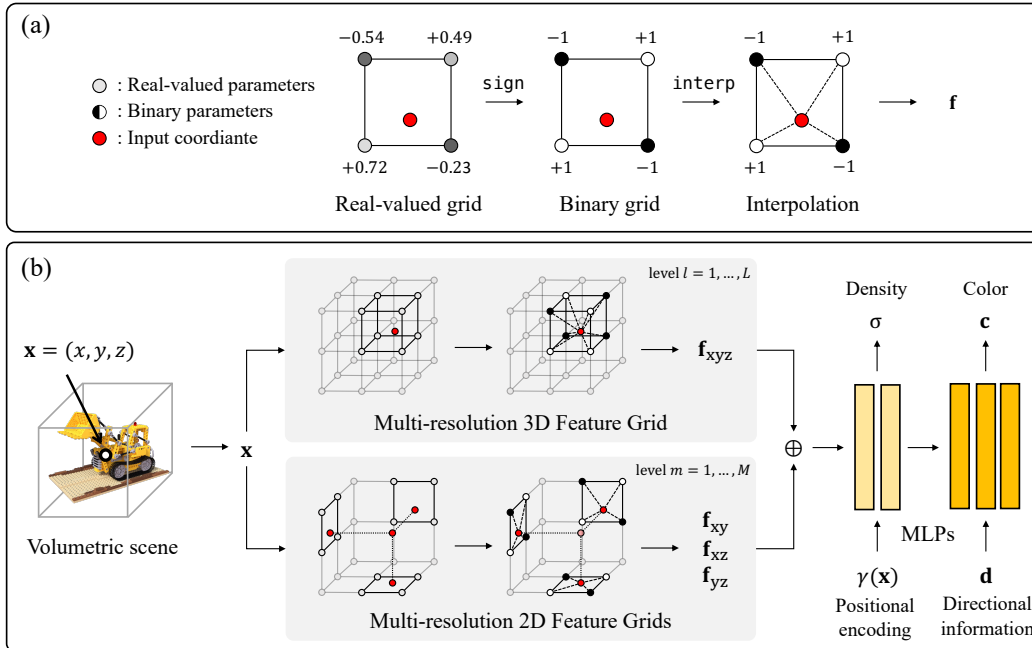


Figure 1: Illustration of overall framework: (a) binary feature encoding, and (b) binary radiance field representation. (a) Our binary feature encoding begins with applying binarization operation to the real-valued grid. Next, we linearly interpolate the binary parameters to obtain feature values. (b) Our radiance field representation comprises a 3D and three 2D feature grids. Given a 3D coordinate, the corresponding feature values are computed from each grid using binary feature encoding. The concatenated feature values are then fed as input to shallow density MLP with positional encoded coordinates. Then we can obtain the density value and embedding features that are further provided as input to shallow color MLPs to acquire color value.

decides the total storage size of the radiance field representation. Therefore, we need to consider an efficient data structure.

## 4 Method

In this section, we introduce *binary radiance fields* that require only a small storage space by adopting binary feature grids. Fig. 1 shows the overall scheme of our radiance field reconstruction. We first introduce how to encode the binary parameters in the feature grid during optimization. Furthermore, we present our 2D-3D hybrid feature grid, which enhances the feature encoding by leveraging the strengths of both 2D plane and 3D voxel.

### 4.1 Binarization

**Binarization of learnable parameter** The binarization procedure of real-valued variables is achieved using a deterministic binarization operator [21], the sign function, which transforms a real-valued variable into either +1 or -1:

$$\theta' = \text{sign}(\theta) = \begin{cases} +1 & \text{if } \theta \geq 0, \\ -1 & \text{otherwise,} \end{cases} \quad (4)$$

where  $\theta$  denotes the real-valued variable, and  $\theta'$  represents binary variable.

During training, we maintain and update real-valued parameters rather than directly learning binary parameters. However, since the derivative of the sign function is zero almost everywhere, we cannot use traditional backpropagation to compute gradients for real-valued parameters. Instead, we use the

straight-through estimator (STE) [38], which is a simple but effective technique for backpropagating through threshold functions (e.g., the sign function):

$$\frac{\partial \mathcal{L}}{\partial \theta} = \frac{\partial \mathcal{L}}{\partial \theta'} \mathbb{1}_{|\theta| \leq 1}, \quad (5)$$

where  $\mathcal{L}$  is the loss function. This strategy allows us to maintain the gradient flow and ensure the differentiability of our framework. Note that we stop propagating gradients when  $\theta$  is a large value. This also constrains the value to the range  $\{-1, 1\}$  preventing the divergence of the scale.

**Binary feature encoding** We propose a technique to optimize binary feature encoding, a feature encoding scheme with binary parameters constrained to either  $+1$  or  $-1$ . Instead of real-valued parameters, binary parameters are used for encoding local features in a specific data structure, which are then employed to represent the radiance fields. While real-valued parameters require expensive floating-point data for representation, binary parameters can be expressed in a single bit (1-bit), leading to a significant reduction in storage overhead. Here, we describe how to implement this strategy in the feature grid  $\Phi_\theta$ . We first adopt binarization operation, described in Eq. 4, to the real-valued grid parameter  $\theta$ :

$$\theta' = \text{sign}(\theta) \rightarrow \Phi_{\theta'} = \text{sign}(\Phi_\theta), \quad (6)$$

where  $\theta'$  denotes the binary grid parameter of binary feature grid  $\Phi_{\theta'}$ . Next, we linearly interpolate these binary parameters depending on the given coordinate  $\mathbf{x}$ :

$$\mathbf{f} = \text{interp}(\mathbf{x}, \Phi_{\theta'}) = \text{interp}(\mathbf{x}, \text{sign}(\Phi_\theta)), \quad (7)$$

where  $\mathbf{x}$  is an input coordinate, and  $\mathbf{f}$  denotes the encoded feature value. We utilize the STE [38] to propagate the gradients into the feature grid and update the grid parameters, as described in Eq. 5.

Now, our system is capable of training the feature encoding using binary parameters. This enables us to represent the feature grid with compact data, instead of using expensive floating-point data (16-bit or 32-bit). As a result, there is a tremendous reduction in the total storage size, making our radiance field representation storage-efficient.

## 4.2 Radiance Field Representation

For effective binary feature encoding, we design our multi-resolution feature grids with a 3D voxel grid  $\Phi_{\theta_{xyz}}$ , and three additional multi-resolution 2D planes  $\Phi_{\theta_{xy}}$ ,  $\Phi_{\theta_{xz}}$ ,  $\Phi_{\theta_{yz}}$ , designated to capture features along  $z$ -,  $y$ -, and  $x$ -axis respectively, inspired by NVP [39]. Upon this architectural design, we efficiently encode the local features and use them as inputs of MLPs to predict color and density that represents the radiance fields via volumetric rendering. Note that all feature grids are implemented using a hash encoding [20] for efficiency.

**2D-3D hybrid multi-resolution feature grid** We intend two types of feature grids to contain the feature information in different manners. Despite the effectiveness of the 3D feature grid, the 3D grid is more severely impacted by hash collisions at higher resolutions [20], which leads to limited performance. Thus, we still need to supplement fine-grained components to improve the performance further and incorporate 2D feature grids that alleviate hash collision impact. Since the 3D feature grid encodes the main components, the 2D feature grids efficiently reinforce the feature information with fewer parameters.

**Feature evaluation** Here, we describe the details of binary feature encoding processes to derive the local features, based on an input 3D coordinate  $\mathbf{x} = (x, y, z)$ .

For the 3D feature grid, we compute the local feature by tri-linearly interpolating binary parameters for each level of resolutions, and concatenating them:

$$\mathbf{f}_{xyz} = \{\text{interp}(\mathbf{x}, \text{sign}(\Phi_{\theta_{xyz}}^l))\}_{l=1}^L, \quad (8)$$

where  $\mathbf{f}_{xyz}$  is the computed feature from the 3D grid,  $l$  denotes the grid level and  $L$  indicates the number of grid levels.

In a different way, we perform the binary feature encoding across each axis for the 2D feature grids. Firstly, we project the 3D coordinate  $\mathbf{x}$  along each axis to obtain the projected 2D coordinates

$\mathbf{x}_{xy} = (x, y)$ ,  $\mathbf{x}_{xz} = (x, z)$ , and  $\mathbf{x}_{yz} = (y, z)$ . Next, we adopt bi-linear interpolation to extract features from these three projected 2D coordinates. Then, we acquire the feature value for each level of resolutions and concatenate them:

$$\mathbf{f}_{xy} = \{\text{interp}(\mathbf{x}_{xy}, \text{sign}(\Phi_{\theta_{xy}}^m))\}_{m=1}^M, \quad (9)$$

where  $\mathbf{f}_{xy}$  is the computed feature from the 2D grid across  $z$ -axis,  $m$  denotes the grid level, and  $M$  indicates the number of grid levels. The feature encoding steps for other features  $\mathbf{f}_{xz}$  and  $\mathbf{f}_{yz}$  operate in the similar manner.

**Network architecture** Finally, all these features are concatenated as  $\mathbf{f}$  and fed into MLPs to predict the color  $\mathbf{c}$  and density values  $\sigma$ . We utilize two MLPs each for density prediction and color prediction:

$$\mathbf{f} = \{\mathbf{f}_{xyz}, \mathbf{f}_{xy}, \mathbf{f}_{xz}, \mathbf{f}_{yz}\}, \quad (\sigma, \mathbf{e}) = \text{MLP}_{\text{density}}(\gamma(\mathbf{x}), \mathbf{f}), \quad \mathbf{c} = \text{MLP}_{\text{color}}(\mathbf{e}, \mathbf{d}), \quad (10)$$

where  $\mathbf{e}$  presents embedded feature and  $\gamma(\mathbf{x})$  is the sinusoidal positional encoding [1].

### 4.3 Loss

**Reconstruction loss** According to the volumetric rendering process described in Sec. 3, we can render the RGB pixel values along the sampled rays and optimize them through the color and density values in Eq. 10:

$$\mathcal{L}_{\text{recon}} = \sum_{\mathbf{r} \in \mathcal{R}} \|\hat{C}(\mathbf{r}) - C(\mathbf{r})\|_2^2, \quad (11)$$

where  $\mathbf{r}$  denotes the sampled ray encouraged by the occupancy grid. The efficient ray sampling through the occupancy grid allows us to focus on non-empty space.

**Sparsity loss** For accelerating the rendering speed, it is important to model the volumetric scene sparsely to skip the ray sampling in the empty area using the occupancy grid. Thus, we regularize the sparsity with Cauchy loss [15, 40]:

$$\mathcal{L}_{\text{sparsity}} = \sum_{i,k} \log(1 + 2\sigma(\mathbf{r}_i(t_k))^2). \quad (12)$$

The overall training loss for our radiance field model is defined as  $\mathcal{L} = \mathcal{L}_{\text{recon}} + \lambda_{\text{sparsity}} \mathcal{L}_{\text{sparsity}}$ , where  $\lambda_{\text{sparsity}}$  is the hyper-parameter for sparsity loss. We set  $\lambda_{\text{sparsity}} = 2.0 \times 10^{-5}$  in this work.

## 5 Experiments

We conduct experiments on various benchmark datasets to verify the compactness of our radiance field representation. We evaluate the quantitative and qualitative results against prior works and analyze different architectural design choices.

### 5.1 Experimental Settings

**Datasets** We adopt representative benchmark novel-view synthesis datasets. We use two synthetic datasets: the Synthetic-NeRF dataset [1] and the Synthetic-NSVF dataset [13]. Both datasets consist of eight object scenes rendered with 100 training views and 200 test views at a resolution of  $800 \times 800$  pix. We also employ the Tanks and Temples dataset [41] that consists of five real-world captured scenes whose backgrounds are masked [13]. The training and test views are rendered at a resolution of  $1920 \times 1080$  pix.

**Baselines** We have three types of baseline methods, (a) data structure-based methods, (b) compression-based methods, and (c) implicit-based methods. Firstly, we compare our radiance fields with state-of-the-art radiance field representations adopting efficient data structures (DVGO [11, 12], Plenoxels [15], TensorRF [17], CCNeRF [18], Instant-NGP [20], and K-Planes [19]), which succeed to reconstruct high-quality 3D scenes with fast convergence speed. Specifically, we are interested in



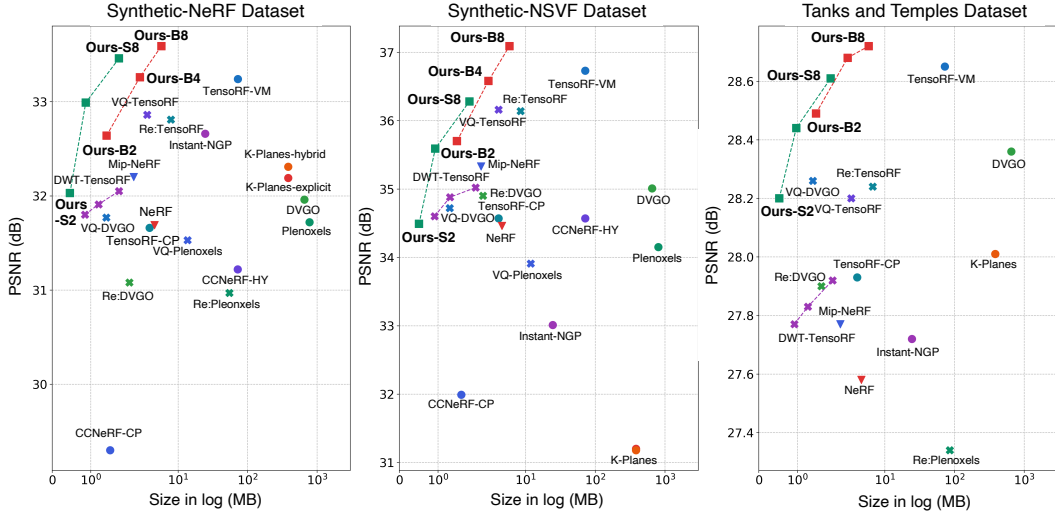


Figure 2: Comparison with baseline radiance field models on the Synthetic-NeRF dataset, Synthetic-NSVF dataset, and Tanks and Temples dataset. We utilize different dot shapes depending on the model categories: squares (■) for our models, circles (●) for data structure-based models, crosses (✕) for compression-based models, and triangles (▼) for implicit-based models.

the models that demonstrate stable performance across multiple datasets and can train within one hour when running on a conventional single GPU. Moreover, we evaluate the compression methods that require post-optimization steps (Re:NeRF [34] and VQRF [36]) and masked wavelet transform (DWT-NeRF [37]) to compress existing voxel-based models. Furthermore, we also compare with representative implicit radiance field models (NeRF [1] and mip-NeRF [24]).

**Implementation details** We implement our feature grid using hash encoding [20]. We use 16 levels of multi-resolution 3D feature grids with resolutions from 16 to 1024, while each grid includes up to  $T_{3D}$  feature vectors. We also utilize four levels of multi-resolution 2D feature grids with resolutions from 64 to 512, while each grid includes up to  $T_{2D}$  feature vectors. We use  $\{\log_2(T_{2D}), \log_2(T_{3D})\} = \{15, 17\}$  for our small model denoting Ours-S and  $\{\log_2(T_{2D}), \log_2(T_{3D})\} = \{17, 19\}$  for our base model denoting Ours-B. Our model variants are scaled by the dimension of feature vectors per level of 2, 4, and 8. For instance, **Ours-B2** denotes a base variant with feature dimension  $F = 2$ . We exploit two types of MLPs with 128-channel hidden layers and rectified linear unit activation on them, one for density prediction with one hidden layer and another for color prediction with two hidden layers. The total storage capacity of MLPs varies from 0.06 to 0.11 MB, depending on the input feature dimension. The spherical harmonics basis function is used to encode the directional information. Our implementation is based on Instant-NGP [20] using the occupancy grid implemented in NerfAcc [42]. We optimize all our models for 20K iterations on a single GPU (NVIDIA RTX A6000). It takes approximately 6, 9, and 14 min of average time to train scenes of the Synthetic-NeRF dataset for Ours-B2 to Ours-B8 models, respectively. We use the Adam [43] optimizer with an initial learning rate of 0.01, which we decay at 15K and 18K iterations by a factor of 0.33. Furthermore, we adopt a warm-up stage during the first 1K iterations to ensure stable optimization.

## 5.2 Comparison

We measured the storage size of each method and evaluated the reconstruction quality (PSNR, SSIM) on various datasets. Note that we present the average scores of all scenes in each dataset; scene-wise full scores are reported in the appendix. Fig. 2 summarizes quantitative evaluations of our radiance field representation, compared to baseline data structure-based, compression-based methods, and implicit-based methods.

**Data structure-based approaches** Fig. 3 shows the qualitative evaluations of our model, compared to data structure-based methods. Our method successfully demonstrates superior reconstruction performance against SOTA data structure-based methods with comparable training time and remarkably small storage size; especially Ours-S2 requires only within 0.5 MB. While baseline approaches

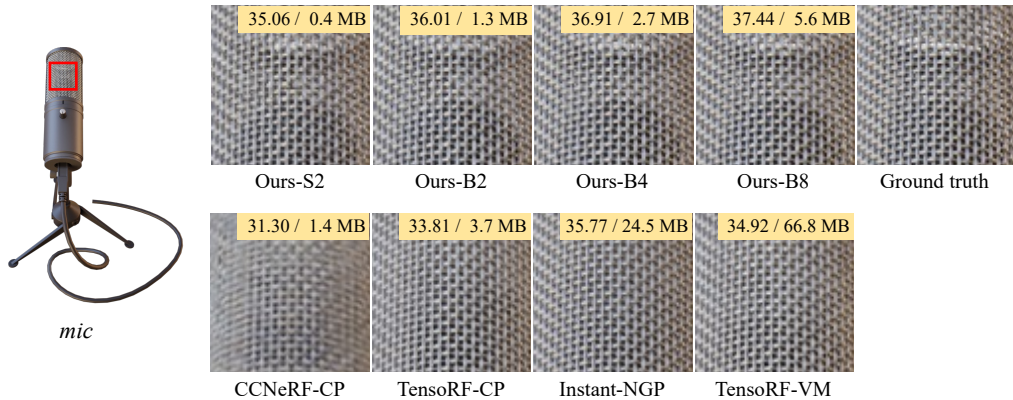


Figure 3: Qualitative comparison of reconstruction quality using the *mic* scene of the NeRF-Synthetic dataset. For each subfigure, PSNR and storage size are shown on the right upper.

require large storage space to achieve high performance, all our models are sufficient to exceed them by less than 6 MB. In particular, Ours-B2 outperforms the reconstruction quality of almost baselines with a much smaller storage size of within 1.5 MB. It takes 6.1 min to accomplish this without any temporal burden to train our model in a compact manner. Although our small models are enough to accomplish outstanding performance, we adopt larger models to attain higher quality. As a result, both Ours-B4 and Ours-B8 jump to excessive reconstruction quality, outperforming state-of-the-art models. Accordingly, the results indicate that our model contains the most storage-efficient data structure for radiance field representation, which also does not require much computational cost.

**Compression-based approaches** We also compare our models with SOTA compression-based methods. Although these approaches make the existing data structure-based models (e.g., DVGO, Plenoxels, and TensoRF-VM) highly compact by compressing the optimized model, our binary feature encoding model outperforms highly compressed data structure-based models in terms of reconstruction performance and storage usage. Specifically, while compressed TensoRF-VM models (Re:TensoRF-High [34], VQ-TensoRF [36], and DWT-TensoRF [37]) preserve most high performance among these compression works, Ours-B4 model has superior reconstruction quality only with 2.8 MB of storage capacity, which is smaller than the compressed TensoRF-VM models. Consequently, the results verify that our binary radiance field models accomplish higher compactness than compression-based models, even without any post-optimization procedure to compress the storage capacity.

**Implicit-based approaches** In addition, we evaluate implicit representations with a few number of parameters due to the efficient structure of MLPs. Although their simple structure results in a small storage size, our models achieve significantly higher performance with a similar storage size.

### 5.3 Ablation Study

**Feature grid design** We analyze the impact of the feature grid designs for scene representation and verify that our 2D-3D hybrid feature grid effectively improves the reconstruction performance. We compare three architectures with similar sizes: (a) tri-plane representation, (b) voxel representation, and (c) our 2D-3D hybrid representation. Table 1 demonstrates the effectiveness of our 2D-3D hybrid representation. Compared to the tri-plane and voxel grid, our hybrid feature grid enhances the radiance field reconstruction quality with a similar number of parameters. As a result, this confirms that our architectural choice for the feature grid allows us to achieve more compact feature encoding.

**Sparsity loss** We investigate the effectiveness of sparsity loss that accelerates the rendering speed by regularizing the radiance fields more sparsely. We evaluate the train time and inference speed of our radiance field model, according to the use of sparsity loss. As shown in Table 2, we can improve the rendering time in both training and inference with a minor decrease in reconstruction quality. In particular, we can accelerate the 23% of rendering speed for Ours-B8 model by adopting sparsity



Table 1: Ablation study on the feature grid design. Results are averaged over all scenes of the Synthetic-NeRF dataset. We highlight the best scores in **bold**.

Design	# Params	PSNR $\uparrow$	SSIM $\uparrow$
Tri-plane (only 2D)	13.7 M	31.44	0.949
Voxel (only 3D)	13.6 M	32.35	0.956
Hybrid (2D + 3D)	13.2 M	<b>32.64</b>	<b>0.958</b>

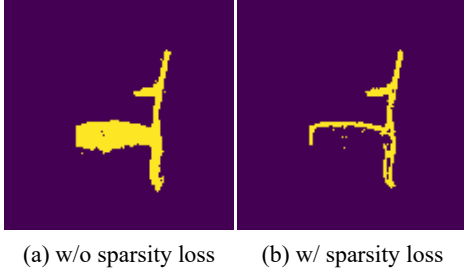


Figure 4: Visualization of a 2D slice of occupancy grid for *chair* scene of the Synthetic-NeRF dataset according to the use of sparsity loss  $\mathcal{L}_{\text{sparsity}}$ .

Table 3: Quantitative evaluations of dynamic scene reconstruction using binary feature encoding. Results are averaged over all scenes of D-NeRF dataset [6] and HyperNeRF dataset [8].  $\dagger$  denotes that binary feature encoding is applied.

Method	D-NeRF [6] (synthetic)		
	Size (MB) $\downarrow$	PSNR $\uparrow$	SSIM $\uparrow$
TiNeuVox-S	7.63	31.03	0.957
TiNeuVox-S $\dagger$	0.59	28.68	0.938
TiNeuVox-B	47.51	33.02	0.972
TiNeuVox-B $\dagger$	3.88	31.23	0.961

Method	HyperNeRF [8] (real)		
	Size (MB) $\downarrow$	PSNR $\uparrow$	MS-SSIM $\uparrow$
TiNeuVox-B	47.85	24.20	0.835
TiNeuVox-B $\dagger$	3.90	23.87	0.826

Table 2: Ablation study on the use of sparsity loss. We report train time and inference speed with reconstruction quality. Results are averaged over all scenes of the Synthetic-NeRF dataset.

	Train $\downarrow$	Inference $\uparrow$	PSNR $\uparrow$	SSIM $\uparrow$
Ours-B2 (w/o $\mathcal{L}_{\text{sparsity}}$ )	6.4 m	3.3 fps	32.69	0.958
Ours-B2 (w/ $\mathcal{L}_{\text{sparsity}}$ )	6.1 m	3.8 fps	32.64	0.958
Ours-B8 (w/o $\mathcal{L}_{\text{sparsity}}$ )	14.7 m	2.2 fps	33.60	0.964
Ours-B8 (w/ $\mathcal{L}_{\text{sparsity}}$ )	13.9 m	2.7 fps	33.59	0.964

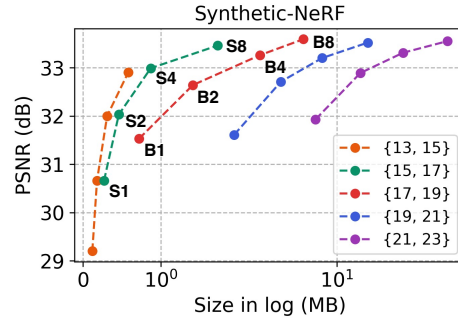


Figure 5: Ablation study on the hash table size. Results are averaged over all scenes of the Synthetic-NeRF dataset.

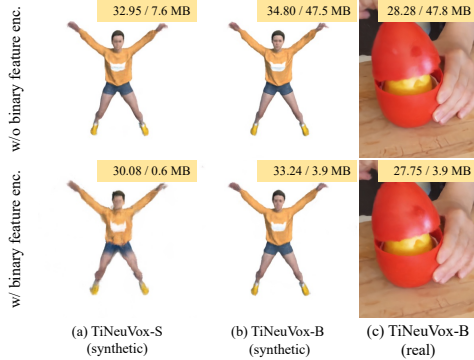


Figure 6: Qualitative evaluations of dynamic scene reconstruction on the use of binary feature encoding. Original (up) and binary feature encoding (bottom). PSNR and storage size are shown on the right upper.

loss. The visualization of the occupancy grid, including the bitmap for the empty or non-empty area, also demonstrates that our model is trained sparsely due to sparsity loss, as shown in Fig. 4.

**Hash table size** We use hash encoding to construct our 2D/3D feature grids, which are restricted in their scale by the hash table size and the number of feature vectors per level. In other words, we can further reduce the storage size for compactness or increase the storage size to improve performance by scaling the number of feature vectors in the hash table. As shown in Fig. 5, we evaluate the storage size and the reconstruction performance of different hash table sizes  $\{\log_2(T_{2D}), \log_2(T_{3D})\}$ , where  $T_{2D}$  and  $T_{3D}$  denote the hash table size of the 2D and 3D grid, respectively.

## 5.4 Applications

**Dynamic scene reconstruction** We finally adopted our binarization strategy in dynamic scene reconstruction. We employ TiNeuVox [22], as our base model, one of the most efficient approaches

which utilizes time-aware voxel features. Instead of conventional feature encoding for the voxel grid, we apply the binary feature encoding on the time-aware voxel features and this leads to a highly compact reconstruction of dynamic scenes, even in 0.6 MB of storage space for the synthetic *jumpingjacks* scene. Table 3 and Fig. 6 demonstrate that our approach is easily applicable to various feature encoding tasks, and it enables remarkably efficient representation in terms of storage size.

## 6 Conclusion

In this work, we have introduced *binary radiance fields*, a storage-efficient radiance field representation that significantly reduces the storage capacity by adopting binary feature encoding. Our experiments have verified that our approach is the most storage-efficient representation outperforming SOTA data structure-based models, compression-based models, and implicit-based models in terms of reconstruction quality and storage consumption. This capability enables us to access numerous radiance fields without a storage burden and leads to the expansion of the applications, such as dynamic scenes.

**Limitations** Although we demonstrated the practicality of our approach, our unoptimized implementation takes slightly longer training time than our un-binarized counterpart (such as Instant-NGP [20]), so there is room for improvement. Despite the binarization of learnable parameters, any bit-wise operations in multi-layered perception would lead to more efficient computation, requiring fewer GPU resources. Our approach is not intended for real-time rendering, so boosting rendering speed by adopting the baking process would be future work.

## 7 Acknowledgments and Disclosure of Funding

The authors acknowledge the support provided by Samsung Advanced Institute of Technology (SAIT). This work was supported by IITP grants (RS-2023-00227993: Detailed 3D reconstruction for urban areas from unstructured images, No.2022-0-00290: Visual Intelligence for Space-Time Understanding and Generation based on Multi-layered Visual Common Sense, No.2019-0-01906: AI Graduate School Program at POSTECH, No.2021-0-01343: AI Graduate School Program at Seoul National University) funded by Korea government (MSIT).

## References

- [1] Ben Mildenhall, Pratul P Srinivasan, Matthew Tancik, Jonathan T Barron, Ravi Ramamoorthi, and Ren Ng. Nerf: Representing scenes as neural radiance fields for view synthesis. *Communications of the ACM*, 65(1):99–106, 2021.
- [2] Kai Zhang, Gernot Riegler, Noah Snively, and Vladlen Koltun. Nerf++: Analyzing and improving neural radiance fields. *arXiv preprint arXiv:2010.07492*, 2020.
- [3] Jonathan T Barron, Ben Mildenhall, Dor Verbin, Pratul P Srinivasan, and Peter Hedman. Mip-nerf 360: Unbounded anti-aliased neural radiance fields. In *Proceedings of the IEEE/CVF Conference on Computer Vision and Pattern Recognition*, pages 5470–5479, 2022.
- [4] Dor Verbin, Peter Hedman, Ben Mildenhall, Todd Zickler, Jonathan T Barron, and Pratul P Srinivasan. Ref-nerf: Structured view-dependent appearance for neural radiance fields. In *2022 IEEE/CVF Conference on Computer Vision and Pattern Recognition (CVPR)*, pages 5481–5490. IEEE, 2022.
- [5] Yuan-Chen Guo, Di Kang, Linchao Bao, Yu He, and Song-Hai Zhang. Nerfren: Neural radiance fields with reflections. In *Proceedings of the IEEE/CVF Conference on Computer Vision and Pattern Recognition*, pages 18409–18418, 2022.
- [6] Albert Pumarola, Enric Corona, Gerard Pons-Moll, and Francesc Moreno-Noguer. D-nerf: Neural radiance fields for dynamic scenes. In *Proceedings of the IEEE/CVF Conference on Computer Vision and Pattern Recognition*, pages 10318–10327, 2021.
- [7] Keunhong Park, Utkarsh Sinha, Jonathan T Barron, Sofien Bouaziz, Dan B Goldman, Steven M Seitz, and Ricardo Martin-Brualla. Nerfies: Deformable neural radiance fields. In *Proceedings of the IEEE/CVF International Conference on Computer Vision*, pages 5865–5874, 2021.
- [8] Keunhong Park, Utkarsh Sinha, Peter Hedman, Jonathan T Barron, Sofien Bouaziz, Dan B Goldman, Ricardo Martin-Brualla, and Steven M Seitz. Hypernerf: a higher-dimensional representation for topologically varying neural radiance fields. *ACM Transactions on Graphics (TOG)*, 40(6):1–12, 2021.

- [9] Alex Yu, Vickie Ye, Matthew Tancik, and Angjoo Kanazawa. pixelnerf: Neural radiance fields from one or few images. In *Proceedings of the IEEE/CVF Conference on Computer Vision and Pattern Recognition*, pages 4578–4587, 2021.
- [10] Michael Niemeyer, Jonathan T Barron, Ben Mildenhall, Mehdi SM Sajjadi, Andreas Geiger, and Noha Radwan. Regnerf: Regularizing neural radiance fields for view synthesis from sparse inputs. In *Proceedings of the IEEE/CVF Conference on Computer Vision and Pattern Recognition*, pages 5480–5490, 2022.
- [11] Cheng Sun, Min Sun, and Hwann-Tzong Chen. Direct voxel grid optimization: Super-fast convergence for radiance fields reconstruction. In *Proceedings of the IEEE/CVF Conference on Computer Vision and Pattern Recognition*, pages 5459–5469, 2022.
- [12] Cheng Sun, Min Sun, and Hwann-Tzong Chen. Improved direct voxel grid optimization for radiance fields reconstruction. *arXiv preprint arXiv:2206.05085*, 2022.
- [13] Lingjie Liu, Jiatao Gu, Kyaw Zaw Lin, Tat-Seng Chua, and Christian Theobalt. Neural sparse voxel fields. *Advances in Neural Information Processing Systems*, 33:15651–15663, 2020.
- [14] Alex Yu, Ruilong Li, Matthew Tancik, Hao Li, Ren Ng, and Angjoo Kanazawa. Plenotrees for real-time rendering of neural radiance fields. In *Proceedings of the IEEE/CVF International Conference on Computer Vision*, pages 5752–5761, 2021.
- [15] Sara Fridovich-Keil, Alex Yu, Matthew Tancik, Qinhong Chen, Benjamin Recht, and Angjoo Kanazawa. Plenoxels: Radiance fields without neural networks. In *Proceedings of the IEEE/CVF Conference on Computer Vision and Pattern Recognition*, pages 5501–5510, 2022.
- [16] Eric R Chan, Connor Z Lin, Matthew A Chan, Koki Nagano, Boxiao Pan, Shalini De Mello, Orazio Gallo, Leonidas J Guibas, Jonathan Tremblay, Sameh Khamis, et al. Efficient geometry-aware 3d generative adversarial networks. In *Proceedings of the IEEE/CVF Conference on Computer Vision and Pattern Recognition*, pages 16123–16133, 2022.
- [17] Anpei Chen, Zexiang Xu, Andreas Geiger, Jingyi Yu, and Hao Su. Tensorf: Tensorial radiance fields. In *Computer Vision—ECCV 2022: 17th European Conference, Tel Aviv, Israel, October 23–27, 2022, Proceedings, Part XXXII*, pages 333–350. Springer, 2022.
- [18] Jiaxiang Tang, Xiaokang Chen, Jingbo Wang, and Gang Zeng. Compressible-composable nerf via rank-residual decomposition. *arXiv preprint arXiv:2205.14870*, 2022.
- [19] Sara Fridovich-Keil, Giacomo Meanti, Frederik Warburg, Benjamin Recht, and Angjoo Kanazawa. K-planes: Explicit radiance fields in space, time, and appearance. *arXiv preprint arXiv:2301.10241*, 2023.
- [20] Thomas Müller, Alex Evans, Christoph Schied, and Alexander Keller. Instant neural graphics primitives with a multiresolution hash encoding. *ACM Transactions on Graphics (ToG)*, 41(4):1–15, 2022.
- [21] Matthieu Courbariaux, Itay Hubara, Daniel Soudry, Ran El-Yaniv, and Yoshua Bengio. Binarized neural networks: Training deep neural networks with weights and activations constrained to+ 1 or-1. *arXiv preprint arXiv:1602.02830*, 2016.
- [22] Jiemin Fang, Taoran Yi, Xinggang Wang, Lingxi Xie, Xiaopeng Zhang, Wenyu Liu, Matthias Nießner, and Qi Tian. Fast dynamic radiance fields with time-aware neural voxels. In *SIGGRAPH Asia 2022 Conference Papers*, pages 1–9, 2022.
- [23] Liangchen Song, Anpei Chen, Zhong Li, Zhang Chen, Lele Chen, Junsong Yuan, Yi Xu, and Andreas Geiger. Nerfplayer: A streamable dynamic scene representation with decomposed neural radiance fields. *arXiv preprint arXiv:2210.15947*, 2022.
- [24] Jonathan T Barron, Ben Mildenhall, Matthew Tancik, Peter Hedman, Ricardo Martin-Brualla, and Pratul P Srinivasan. Mip-nerf: A multiscale representation for anti-aliasing neural radiance fields. In *Proceedings of the IEEE/CVF International Conference on Computer Vision*, pages 5855–5864, 2021.
- [25] Ricardo Martin-Brualla, Noha Radwan, Mehdi SM Sajjadi, Jonathan T Barron, Alexey Dosovitskiy, and Daniel Duckworth. Nerf in the wild: Neural radiance fields for unconstrained photo collections. In *Proceedings of the IEEE/CVF Conference on Computer Vision and Pattern Recognition*, pages 7210–7219, 2021.
- [26] Zirui Wang, Shangzhe Wu, Weidi Xie, Min Chen, and Victor Adrian Prisacariu. Nerf-: Neural radiance fields without known camera parameters. *arXiv preprint arXiv:2102.07064*, 2021.
- [27] Christian Reiser, Songyou Peng, Yiyi Liao, and Andreas Geiger. Kilonerf: Speeding up neural radiance fields with thousands of tiny mlps. In *Proceedings of the IEEE/CVF International Conference on Computer Vision*, pages 14335–14345, 2021.
- [28] Qiang Zhang, Seung-Hwan Baek, Szymon Rusinkiewicz, and Felix Heide. Differentiable point-based radiance fields for efficient view synthesis. *arXiv preprint arXiv:2205.14330*, 2022.
- [29] Qiangeng Xu, Zexiang Xu, Julien Philip, Sai Bi, Zhixin Shu, Kalyan Sunkavalli, and Ulrich Neumann. Point-nerf: Point-based neural radiance fields. In *Proceedings of the IEEE/CVF Conference on Computer Vision and Pattern Recognition*, pages 5438–5448, 2022.

- [30] Ang Cao and Justin Johnson. Hexplane: a fast representation for dynamic scenes. *arXiv preprint arXiv:2301.09632*, 2023.
- [31] Anpei Chen, Zexiang Xu, Xinyue Wei, Siyu Tang, Hao Su, and Andreas Geiger. Factor fields: A unified framework for neural fields and beyond. *arXiv preprint arXiv:2302.01226*, 2023.
- [32] Fangneng Zhan, Lingjie Liu, Adam Kortylewski, and Christian Theobalt. General neural gauge fields. *arXiv preprint arXiv:2305.03462*, 2023.
- [33] Yoonwoo Jeong, Seungjoo Shin, Junha Lee, Chris Choy, Anima Anandkumar, Minsu Cho, and Jaesik Park. Perfception: Perception using radiance fields. In *Thirty-sixth Conference on Neural Information Processing Systems Datasets and Benchmarks Track*, 2022.
- [34] Chenxi Lola Deng and Enzo Tartaglione. Compressing explicit voxel grid representations: fast nerfs become also small. In *Proceedings of the IEEE/CVF Winter Conference on Applications of Computer Vision*, pages 1236–1245, 2023.
- [35] Towaki Takikawa, Alex Evans, Jonathan Tremblay, Thomas Müller, Morgan McGuire, Alec Jacobson, and Sanja Fidler. Variable bitrate neural fields. In *ACM SIGGRAPH 2022 Conference Proceedings*, pages 1–9, 2022.
- [36] Lingzhi Li, Zhen Shen, Zhongshu Wang, Li Shen, and Liefeng Bo. Compressing volumetric radiance fields to 1 mb. *arXiv preprint arXiv:2211.16386*, 2022.
- [37] Daniel Rho, Byeonghyeon Lee, Seungtae Nam, Joo Chan Lee, Jong Hwan Ko, and Eunbyung Park. Masked wavelet representation for compact neural radiance fields. In *Proceedings of the IEEE/CVF Conference on Computer Vision and Pattern Recognition*, pages 20680–20690, 2023.
- [38] Yoshua Bengio, Nicholas Léonard, and Aaron Courville. Estimating or propagating gradients through stochastic neurons for conditional computation. *arXiv preprint arXiv:1308.3432*, 2013.
- [39] Subin Kim, Sihyun Yu, Jaeho Lee, and Jinwoo Shin. Scalable neural video representations with learnable positional features. *arXiv preprint arXiv:2210.06823*, 2022.
- [40] Peter Hedman, Pratul P Srinivasan, Ben Mildenhall, Jonathan T Barron, and Paul Debevec. Baking neural radiance fields for real-time view synthesis. In *Proceedings of the IEEE/CVF International Conference on Computer Vision*, pages 5875–5884, 2021.
- [41] Arno Knapitsch, Jaesik Park, Qian-Yi Zhou, and Vladlen Koltun. Tanks and temples: Benchmarking large-scale scene reconstruction. *ACM Transactions on Graphics (ToG)*, 36(4):1–13, 2017.
- [42] Ruilong Li, Matthew Tancik, and Angjoo Kanazawa. Nerfacc: A general nerf acceleration toolbox. *arXiv preprint arXiv:2210.04847*, 2022.
- [43] Diederik P Kingma and Jimmy Ba. Adam: A method for stochastic optimization. *arXiv preprint arXiv:1412.6980*, 2014.

## A Experimental Setting of Baselines

We have followed the experimental setting of the configurations released in the official code with minor modifications. We use reported scores in the original paper for Re:NeRF [34] and VQRf [36].

**DVGO** DVGO [11, 12] consists of coarse and fine grids of density and features with a shallow MLP for color prediction. We set the number of voxels in the coarse grids to  $100^3$  and in the fine grids to  $160^3$  for both the density and feature grids. The dimension of features stored in each voxel of the coarse and fine density grid is 1, while in the coarse and fine feature grid, it is 3 and 12, respectively. The shallow MLP has two 128-channel hidden layers with ReLU activation.

**Plenoxels** Plenoxels [15] consists of sparse voxel grids having density values and spherical harmonics coefficients. We set the number of voxels from  $256^3$  to  $512^3$  during training. The dimension of features for density voxel is 1, and for spherical harmonics, the number of coefficients is 27 since we use spherical harmonics of degree 3.

**TensorRF** TensorRF-VM [17] consists of vector and matrix components with a shallow MLP for color prediction. We set the number of voxels from  $128^3$  to  $300^3$  during training. The dimension of features in each cell of vector and matrix components is 48 for density and 144 for color. Similarly, TensorRF-CP [17] consists of only vector components with a shallow MLP for color prediction. We also set the number of voxels from  $128^3$  to  $300^3$  during training. The dimension of features in each cell of vector components is 96 for density and 288 for color. The shallow MLP has two 128-channel hidden layers with ReLU activation.

**CCNeRF** CCNeRF-HY [18] uses a hybrid representation that combines CANDECOMP/PARAFAC (CP) decomposition and Triple Plane (TP) decomposition. We set the number of voxels from  $128^3$  to  $300^3$  during training. CCNeRF-HY has 96 vector components for expressing density, and it has 96 vector components and 64 matrix components for expressing color. Due to the rank-residual learning strategy, we can efficiently reduce the model size by adopting rank truncation that excludes the matrix components for color. Since this model contains only vector components for CP decomposition, we denote this truncated CCNeRF-HY model as CCNeRF-CP in this paper. Note that it differs from the experimental setting of CCNeRF-CP in the original paper, which exclusively employs vector components for optimization like TensorRF-CP.

**Instant-NGP** Instant-NGP [20] consists of a multi-resolution hash grid with two shallow MLPs each for density and color prediction. We set the 16 resolutions of the feature grid from 16 to 2048, the size of hash table  $2^{19}$ , and the feature dimension 2. The density MLP has one 64-channel hidden layer with ReLU activation, and the color MLP has two 64-channel hidden layers with ReLU activation.

**K-Planes** K-Planes [19] consists of multi-resolution planes with resolutions of 128, 256, and 512. Each cell in the planes has a 32-dim feature. K-Planes-hybrid model decodes the features using two shallow MLPs, similar to Instant-NGP [20]. The density MLP has one 64-channel hidden layer with ReLU activation, and the color MLP has two 64-channel hidden layers with ReLU activation. In the K-Planes-explicit model, the features are decoded using an explicit linear decoder.

**NeRF** NeRF [1] consists of an coarse implicit network and an fine implicit network. Each network has eight 256-channel hidden layers with ReLU activation, one additional 256-channel layer with ReLU activation, and one 128-channel layer with ReLU activation.

**Mip-NeRF** Mip-NeRF [24] consists of an implicit network. The network has eight 256-channel hidden layers with shifted Softplus activation, one additional 256-channel layer with shifted Softplus activation, and one 128-channel layer with shifted Softplus activation.

## B Additional Results

### B.1 Quantitative Results

Table 4 summarizes the average scores of quantitative results on the Synthetic-NeRF, Synthetic-NSVF, and Tanks and Temples datasets. Our model successfully outperforms data-structure- and compression-based models for all datasets with highly compact storage sizes. We provide scores of DWT-TensoRF [37] on the Tanks and Temples dataset reported in the original paper since several scenes require large memory of more than 48 GB. The failure of *Lifestyle* scene causes the noticeably worse performance of K-Planes [19] on the Synthetic-NSVF dataset; see Table. 11 & 12.

Table 4: Quantitative results of model size and reconstruction quality on the Synthetic-NeRF dataset, Synthetic-NSVF dataset, and Tanks and Temples dataset. We divide the baselines into data-structure-based models (upper rows) and compression-based (middle rows) models. † denotes that we provide scores reported in the original paper. We denote our small model as Ours-S and our base model as Ours-B. All our models are scaled by the feature dimension  $F$ ; for instance, Ours-B2 denotes a base variant with feature dimension  $F = 2$ . We highlight the **best score** and **second-best score**.

Method	Synthetic-NeRF			Synthetic-NSVF			Tanks and Temples		
	Size↓ (MB)	PSNR↑	SSIM↑	Size↓ (MB)	PSNR↑	SSIM↑	Size↓ (MB)	PSNR↑	SSIM↑
DVGO [11, 12]	655.3	31.96	0.956	653.7	35.01	0.975	652.8	28.36	0.911
Plenoxels [15]	778.2	31.72	0.958	803.6	34.15	0.978	892.8	26.87	0.912
TensoRF-CP [17]	3.9	31.66	0.950	4.1	34.57	0.971	4.0	27.93	0.901
TensoRF-VM [17]	72.4	33.24	0.963	71.6	36.73	0.982	72.5	28.65	0.922
CCNeRF-CP [18]	1.5	29.30	0.937	1.6	31.99	0.950	1.6	26.25	0.873
CCNeRF-HY [18]	72.1	31.22	0.947	71.7	34.57	0.974	73.7	27.62	0.901
Instant-NGP [20]	24.6	32.66	0.958	24.6	33.01	0.973	24.5	27.72	0.926
K-Planes-explicit [19]	384.7	32.19	0.960	383.9	31.20	0.952	383.9	28.01	0.921
K-Planes-hybrid [19]	383.9	32.31	0.961	383.9	31.18	0.951	384.7	28.01	0.921
Re:DVGO-High† [34]	2.0	31.08	0.944	2.5	34.90	0.969	1.6	27.90	0.894
Re:Plenoxels-High† [34]	54.7	30.97	0.944	-	-	-	85.5	27.34	0.896
Re:TensoRF-High† [34]	7.9	32.81	0.956	8.5	36.14	0.978	6.7	28.24	0.907
VQ-DVGO† [36]	1.4	31.77	0.954	1.3	34.72	0.974	1.4	28.26	0.909
VQ-Plenoxels† [36]	13.7	31.53	0.956	11.9	33.91	0.976	14.3	26.73	0.908
VQ-TensoRF† [36]	3.6	32.86	0.960	4.1	36.16	0.980	3.3	28.20	0.913
DWT-TensoRF-S [37]	0.9	31.80	0.953	0.9	34.60	0.972	0.9	27.77	-
DWT-TensoRF-M [37]	1.2	31.91	0.954	1.3	34.88	0.974	1.3	27.83	-
DWT-TensoRF-L [37]	1.7	32.05	0.955	2.0	35.02	0.975	1.9	27.92	-
NeRF [1]	4.6	31.69	0.951	4.6	34.46	0.967	4.6	27.58	0.902
Mip-NeRF [24]	2.3	32.20	0.960	2.3	35.33	0.971	2.3	27.77	0.901
Ours-S2	0.5	32.03	0.954	0.5	34.48	0.972	0.5	28.20	0.910
Ours-S4	0.9	32.99	0.960	0.9	35.59	0.978	1.0	28.44	0.914
Ours-S8	1.7	33.46	0.963	1.8	36.28	0.981	1.9	28.61	0.920
Ours-B2	1.4	32.64	0.958	1.5	35.70	0.978	1.6	28.49	0.917
Ours-B4	2.8	33.26	0.962	2.9	36.58	0.982	3.1	28.68	0.922
Ours-B8	5.8	33.59	0.964	5.9	37.09	0.984	6.0	28.72	0.925

### B.2 Training Time

We also evaluate the training time for each method. Fig. 7 shows that our method has a comparable convergence speed to SOTA fast radiance field models.

### B.3 Inference Speed

Additionally, we compare the inference speed of our model with baselines. Fig. 8 demonstrates that our method has a comparable rendering speed to SOTA fast radiance field models.



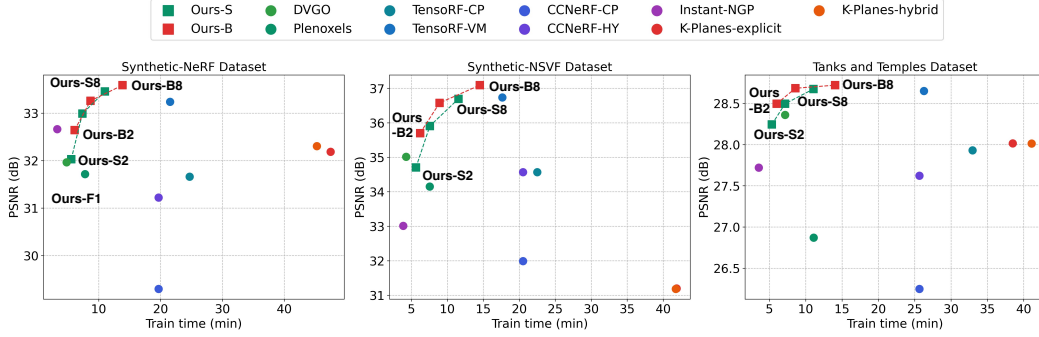


Figure 7: Illustration of the training time and reconstruction quality (PSNR) of each method on the Synthetic-NeRF dataset, Synthetic-NSVF dataset, and Tanks and Temples dataset.

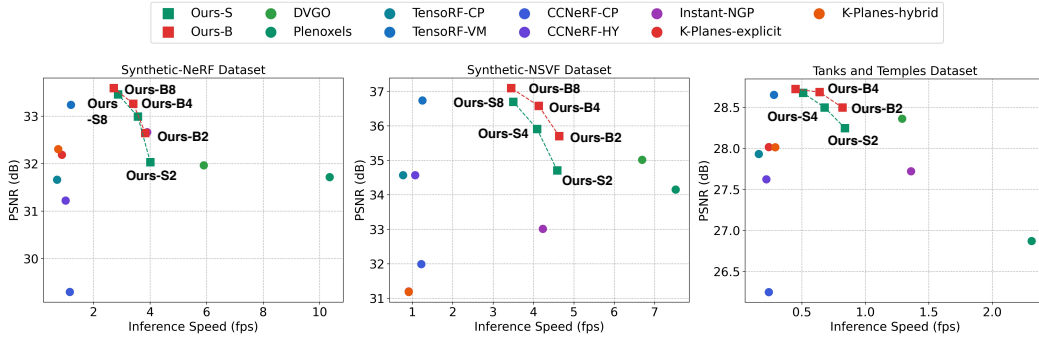


Figure 8: Illustration of the inference speed (fps) and reconstruction quality (PSNR) of each method on the Synthetic-NeRF dataset, Synthetic-NSVF dataset, and Tanks and Temples dataset.

## B.4 Qualitative Results

Fig. 11, 12, and 13 demonstrate the qualitative results on each scene of the Synthetic-NeRF dataset, Synthetic-NSVF dataset, and Tanks and Temples dataset, respectively. We report the rendering images of our method with the cropped area.

## B.5 Ablation Study

**Feature grid design** Table 5 shows the scores of the ablation study on the feature grid design. With a similar number of parameters, our 2D-3D hybrid feature grid design has superior performance on various datasets compared to tri-plane and voxel representation.

Table 5: Ablation study on the feature grid design. The experiments are conducted on the Synthetic-NeRF dataset, Synthetic-NSVF dataset, and Tanks and Temples dataset.

Design	# Params	Synthetic-NeRF		Synthetic-NSVF		Tanks and Temples	
		PSNR $\uparrow$	SSIM $\uparrow$	PSNR $\uparrow$	SSIM $\uparrow$	PSNR $\uparrow$	SSIM $\uparrow$
Tri-plane (only 2D)	13.7 M	31.44	0.949	34.33	0.971	27.97	0.904
Voxel (only 3D)	13.6 M	32.35	0.956	35.10	0.975	28.35	0.912
Hybrid (2D + 3D)	13.2 M	<b>32.64</b>	<b>0.958</b>	<b>35.70</b>	<b>0.978</b>	<b>28.49</b>	<b>0.917</b>

**Hash table size** Table 6 reports the scores of the ablation study on the hash table size. We can further reduce the storage size of our model by using a smaller size of the hash table, but it might lead to a decline in the reconstruction quality. Also, we can achieve higher performance by increasing the

hash table size, leading to a larger storage size. In this work, we use  $\{2^{15}, 2^{17}\}$  and  $\{2^{17}, 2^{19}\}$  size of hash tables as our small and base configuration, respectively.

Table 6: Ablation study on the hash table size. The experiments are conducted on the Synthetic-NeRF dataset.

$\{T_{2D}, T_{3D}\}$	$F = 1$		$F = 2$		$F = 4$		$F = 8$	
	Size (MB)↓	PSNR↑	Size (MB)↓	PSNR↑	Size (MB)↓	PSNR↑	Size (MB)↓	PSNR↑
$\{2^{13}, 2^{15}\}$	0.12	29.20	0.18	30.66	0.31	32.00	0.58	32.90
$\{2^{15}, 2^{17}\}$	0.27	30.66	0.46	32.03	0.87	32.99	1.73	33.46
$\{2^{17}, 2^{19}\}$	0.72	31.53	1.41	32.64	2.83	33.26	5.76	33.59
$\{2^{19}, 2^{21}\}$	1.94	31.61	3.99	32.71	7.84	33.20	16.61	33.52
$\{2^{21}, 2^{23}\}$	7.05	31.93	14.70	32.89	29.65	33.31	61.35	33.55

## B.6 Dynamic Scene Reconstruction

Table 7 and 8 present full scores and Fig. 9 and 10 show the qualitative results of the dynamic scene reconstruction. We apply binary feature encoding to TiNeuVox [22] and compare our model with original model.

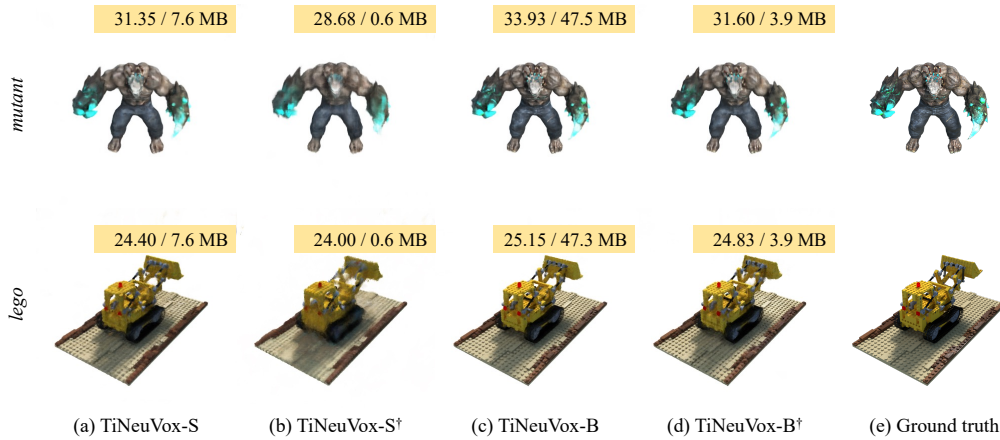


Figure 9: Qualitative results on each scene of the D-NeRF dataset. † denotes that binary feature encoding is applied. PSNR and storage size are shown on the upper right side in each subfigure.

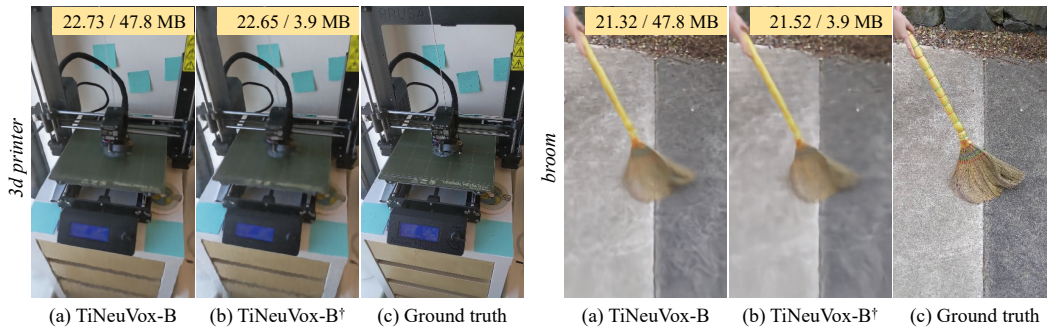


Figure 10: Qualitative results on each scene of the HyperNeRF dataset. † denotes that binary feature encoding is applied. PSNR and storage size are shown on the upper right side in each subfigure.

Table 7: Quantitative results of storage size and reconstruction quality (PSNR, SSIM, LPIPS) on each scene of the D-NeRF dataset. † denotes that binary feature encoding is applied.

Method	<i>bouncingballs</i>	<i>hellwarrior</i>	<i>hook</i>	<i>jumpingjacks</i>	<i>lego</i>	<i>mutant</i>	<i>standup</i>	<i>trex</i>	Avg.
PSNR↑									
TiNeuVox-S	39.34	27.07	29.60	32.95	24.40	31.35	33.50	30.04	31.03
TiNeuVox-S†	36.26	24.54	26.87	30.08	24.00	28.68	30.36	28.62	28.68
TiNeuVox-B	41.09	28.27	31.86	34.80	25.15	33.93	36.12	32.97	33.02
TiNeuVox-B†	39.18	26.86	29.47	33.24	24.83	31.60	33.79	30.86	31.23
SSIM↑									
TiNeuVox-S	0.988	0.954	0.954	0.975	0.886	0.961	0.977	0.958	0.957
TiNeuVox-S†	0.981	0.935	0.928	0.960	0.853	0.942	0.963	0.946	0.938
TiNeuVox-B	0.992	0.965	0.972	0.983	0.921	0.977	0.986	0.979	0.972
TiNeuVox-B†	0.989	0.955	0.954	0.976	0.906	0.964	0.978	0.964	0.961
LPIPS↓									
TiNeuVox-S	0.054	0.080	0.068	0.042	0.117	0.049	0.030	0.059	0.062
TiNeuVox-S†	0.092	0.114	0.097	0.068	0.164	0.069	0.052	0.076	0.091
TiNeuVox-B	0.040	0.066	0.045	0.033	0.070	0.030	0.020	0.031	0.042
TiNeuVox-B†	0.054	0.084	0.071	0.046	0.098	0.047	0.033	0.052	0.061
Size (MB)↓									
TiNeuVox-S	7.6	7.6	7.6	7.6	7.7	7.6	7.6	7.6	7.6
TiNeuVox-S†	0.6	0.6	0.6	0.6	0.6	0.6	0.6	0.6	0.6
TiNeuVox-B	47.5	47.5	47.5	47.5	47.3	47.5	47.5	47.5	47.5
TiNeuVox-B†	3.9	3.9	3.9	3.9	3.9	3.9	3.9	3.9	3.9

Table 8: Quantitative results of storage size and reconstruction quality (PSNR, MS-SSIM) on each scene of the HyperNeRF dataset. † denotes that binary feature encoding is applied.

Method	<i>3d printer</i>	<i>broom</i>	<i>chicken</i>	<i>peel-banana</i>	Avg.
PSNR↑					
TiNeuVox-B	22.73	21.32	28.28	24.47	24.20
TiNeuVox-B†	22.65	21.52	27.75	23.54	23.87
MS-SSIM↑					
TiNeuVox-B	0.835	0.694	0.938	0.873	0.835
TiNeuVox-B†	0.835	0.694	0.938	0.836	0.826
Size (MB)↓					
TiNeuVox-B	47.8	47.8	47.8	47.8	47.8
TiNeuVox-B†	3.9	3.9	3.9	3.9	3.9

## B.7 Scene-wise Results

Table 9, 10, 11, 12, 13, and 14 demonstrate the quantitative results on each scene of the Synthetic-NeRF dataset, Synthetic-NSVF dataset, and Tanks and Temples dataset, respectively. We measured the storage size of each method and evaluated the reconstruction quality (PSNR, SSIM, LPIPS) on various datasets.

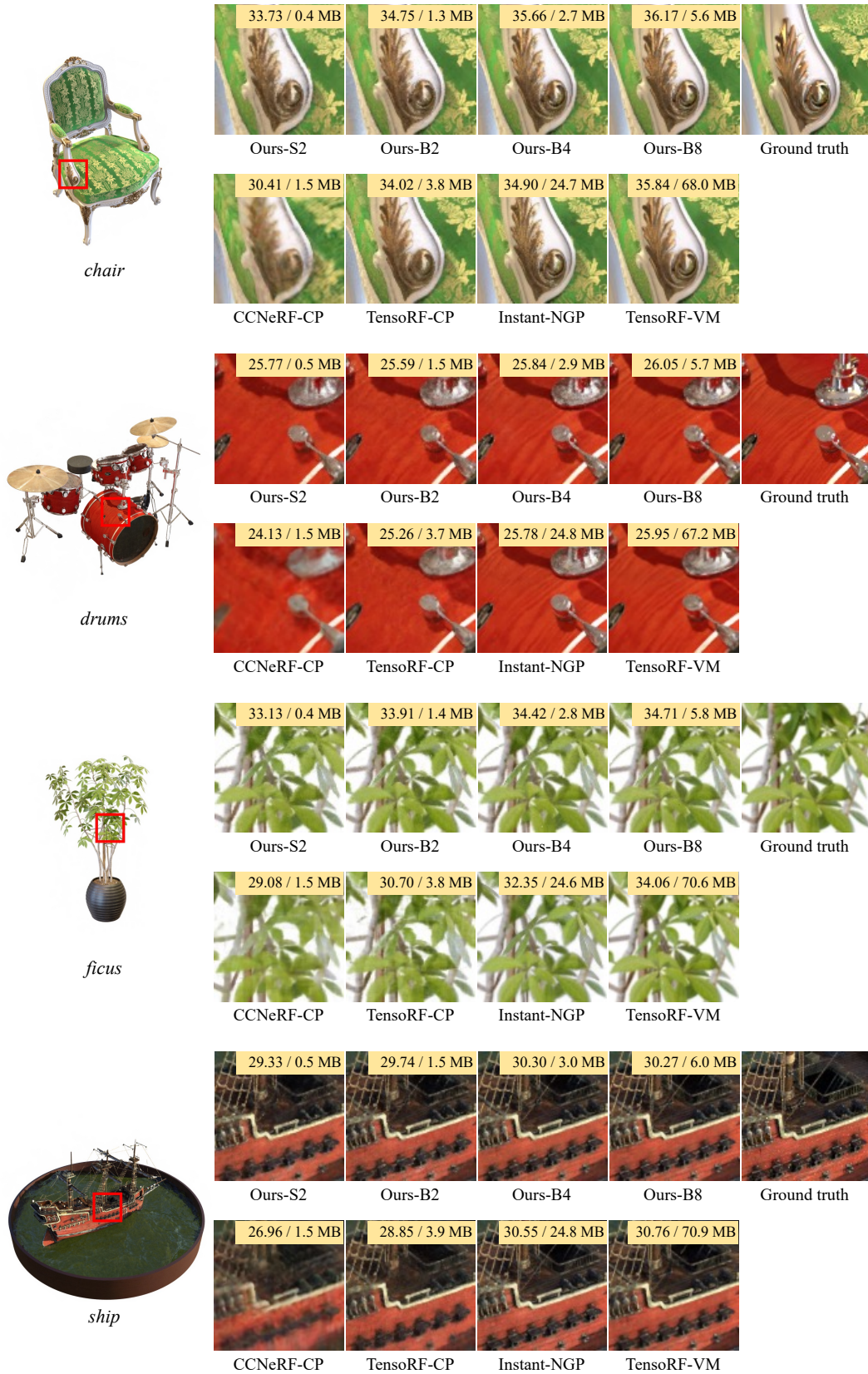


Figure 11: Qualitative results on each scene of the Synthetic-NeRF dataset. PSNR and storage size are shown on the upper right side in each subfigure.



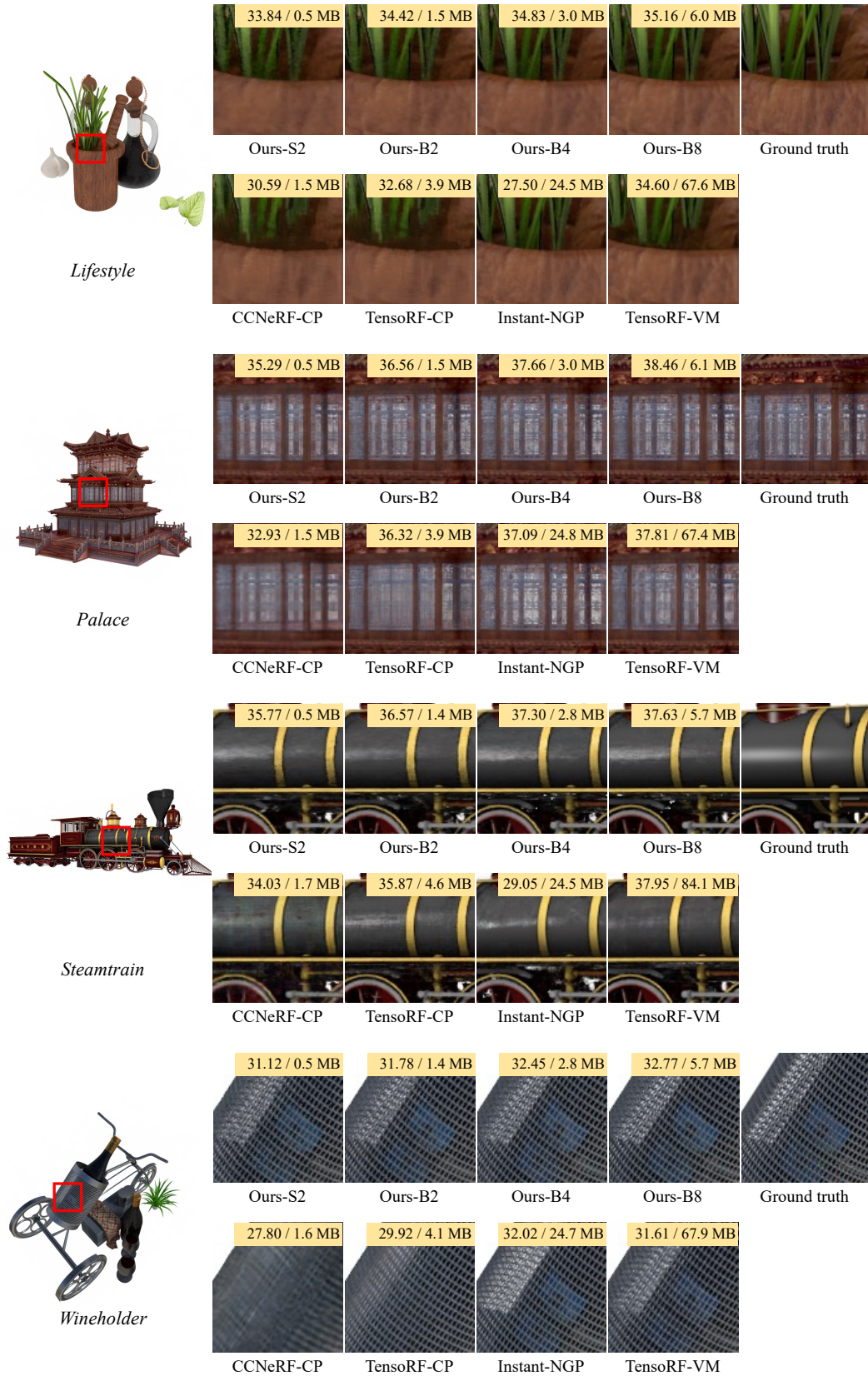


Figure 12: Qualitative results on each scene of the Synthetic-NSVF dataset. PSNR and storage size are shown on the upper right side in each subfigure.

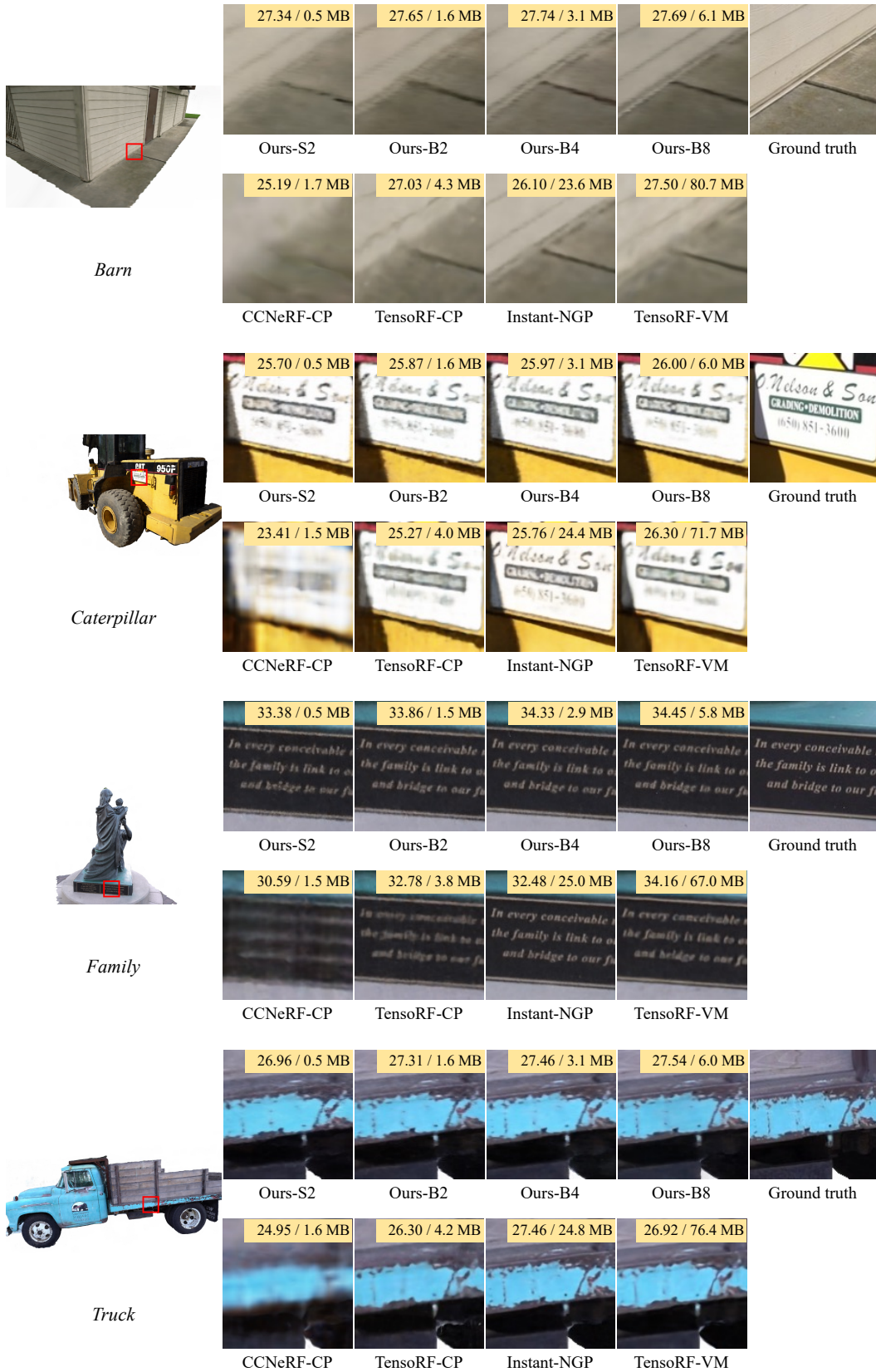


Figure 13: Qualitative results on each scene of the Tanks and Temples dataset. PSNR and storage size are shown on the upper right side in each subfigure.



Table 9: Quantitative results of storage size and reconstruction quality (PSNR) on each scene of the Synthetic-NeRF dataset. We highlight the **best score** and **second-best score**.

Method	<i>chair</i>	<i>drums</i>	<i>ficus</i>	<i>hotdog</i>	<i>lego</i>	<i>materials</i>	<i>mic</i>	<i>ship</i>	Avg.
Size (MB)↓									
DVGO [11, 12]	4.3	4.1	4.6	5.2	4.7	5.2	4.0	6.2	4.8
Plenoxels [15]	7.1	6.9	6.1	8.5	8.0	7.5	5.9	12.3	7.8
TensoRF-CP [17]	22.6	21.1	26.5	23.3	23.9	33.7	21.4	25.1	24.7
TensoRF-VM [17]	24.2	13.4	25.8	18.0	25.4	22.8	23.1	19.6	21.5
CCNeRF-CP [18]	18.3	17.5	20.3	19.9	18.9	23.7	19.0	19.9	19.7
CCNeRF-HY [18]	18.3	17.5	20.3	19.9	18.9	23.7	19.0	19.9	19.7
Instant-NGP [20]	3.6	3.1	2.8	3.5	3.7	2.9	3.3	3.2	3.3
K-Planes-explicit [19]	47.2	48.0	48.0	46.8	47.0	47.9	47.7	47.4	47.5
K-Planes-hybrid [19]	45.5	45.6	45.9	44.3	44.3	45.9	45.4	45.4	45.3
NeRF [1]	4.6	4.6	4.6	4.6	4.6	4.6	4.6	4.6	4.6
Mip-NeRF [24]	2.3	2.3	2.3	2.3	2.3	2.3	2.3	2.3	2.3
Ours-S2	<b>0.4</b>	<b>0.5</b>	<b>0.4</b>	<b>0.5</b>	<b>0.5</b>	<b>0.5</b>	<b>0.4</b>	<b>0.5</b>	<b>0.5</b>
Ours-S4	<b>0.8</b>	<b>0.9</b>	<b>0.8</b>	<b>0.9</b>	<b>0.9</b>	<b>0.9</b>	<b>0.8</b>	<b>1.0</b>	<b>0.9</b>
Ours-S8	1.7	1.7	1.7	1.8	1.8	1.8	1.6	1.8	1.7
Ours-B2	1.3	1.5	1.4	1.4	1.4	1.4	1.3	1.5	1.4
Ours-B4	2.7	2.9	2.8	2.8	2.8	2.8	2.7	3.0	2.8
Ours-B8	5.6	5.7	5.8	5.8	5.8	5.7	5.6	6.0	5.8
PSNR↑									
DVGO [11, 12]	34.26	25.45	32.60	36.78	34.75	29.58	33.22	29.07	31.96
Plenoxels [15]	34.00	25.36	31.83	36.43	34.11	29.13	33.23	29.63	31.72
TensoRF-CP [17]	34.02	25.26	30.70	36.25	34.28	<b>30.13</b>	33.81	28.85	31.66
TensoRF-VM [17]	<b>35.84</b>	25.95	34.06	<b>37.62</b>	<b>36.68</b>	30.11	34.92	<b>30.76</b>	33.24
CCNeRF-CP [18]	30.41	24.13	29.08	33.71	31.04	27.74	31.30	26.96	29.30
CCNeRF-HY [18]	34.28	24.84	30.07	36.10	33.64	28.82	33.58	28.45	31.22
Instant-NGP [20]	34.90	25.78	32.35	36.82	35.57	29.56	35.77	30.55	32.66
K-Planes-explicit [19]	34.85	25.64	31.20	36.66	35.21	29.46	34.02	30.44	32.19
K-Planes-hybrid [19]	34.95	25.67	31.37	36.71	35.69	29.31	34.03	<b>30.71</b>	32.31
NeRF [1]	33.73	25.29	31.26	36.67	33.40	29.95	33.91	29.28	31.69
Mip-NeRF [24]	33.92	25.55	32.55	36.79	34.37	<b>30.19</b>	34.56	29.69	32.20
Ours-S2	33.73	25.77	33.13	36.15	33.91	29.15	35.06	29.33	32.03
Ours-S4	35.02	<b>26.07</b>	34.19	37.03	35.31	29.69	36.65	29.95	32.99
Ours-S8	35.83	<b>26.27</b>	<b>34.64</b>	37.30	36.20	29.93	<b>37.20</b>	30.29	<b>33.46</b>
Ours-B2	34.75	25.59	33.91	36.59	35.06	29.49	36.01	29.74	32.64
Ours-B4	35.66	25.84	34.42	37.13	36.02	29.80	36.91	30.30	33.26
Ours-B8	<b>36.17</b>	26.05	<b>34.71</b>	<b>37.51</b>	<b>36.48</b>	30.09	<b>37.44</b>	30.27	<b>33.59</b>

Table 10: Quantitative results of reconstruction quality (SSIM, LPIPS) on each scene of the Synthetic-NeRF dataset. We highlight the **best score** and **second-best score**.

Method	<i>chair</i>	<i>drums</i>	<i>ficus</i>	<i>hotdog</i>	<i>lego</i>	<i>materials</i>	<i>mic</i>	<i>ship</i>	Avg.
SSIM $\uparrow$									
DVGO [11, 12]	0.977	0.930	0.978	0.980	0.977	0.950	0.983	0.878	0.956
Plenoxels [15]	0.977	0.933	0.976	0.980	0.975	0.949	0.985	0.890	0.958
TensoRF-CP [17]	0.976	0.922	0.965	0.975	0.972	0.950	0.983	0.856	0.950
TensoRF-VM [17]	0.985	0.936	0.983	0.983	0.983	0.952	0.988	0.895	0.963
CCNeRF-CP [18]	0.941	0.902	0.952	0.956	0.944	0.927	0.969	0.826	0.927
CCNeRF-HY [18]	0.977	0.920	0.962	0.975	0.969	0.934	0.984	0.855	0.947
Instant-NGP [20]	0.979	0.931	0.968	0.984	0.979	0.946	0.984	0.895	0.958
K-Planes-explicit [19]	0.981	0.936	0.974	0.981	0.979	0.949	0.988	0.892	0.960
K-Planes-hybrid [19]	0.983	0.938	0.975	0.981	0.982	0.948	0.988	0.896	0.961
NeRF [1]	0.972	0.928	0.970	0.977	0.965	0.952	0.984	0.864	0.951
Mip-NeRF [24]	0.973	0.931	0.976	0.978	0.970	0.955	0.986	0.870	0.955
Ours-S2	0.974	0.930	0.977	0.975	0.968	0.939	0.987	0.880	0.954
Ours-S4	0.981	0.936	0.982	0.979	0.977	0.946	0.990	0.890	0.960
Ours-S8	0.984	0.939	0.984	0.980	0.981	0.950	0.992	0.896	0.963
Ours-B2	0.980	0.930	0.981	0.978	0.976	0.943	0.989	0.888	0.958
Ours-B4	0.984	0.934	0.983	0.980	0.980	0.948	0.991	0.895	0.962
Ours-B8	0.986	0.937	0.984	0.981	0.982	0.951	0.992	0.897	0.964
LPIPS $\downarrow$									
DVGO [11, 12]	0.026	0.079	0.025	0.033	0.026	0.058	0.017	0.160	0.053
Plenoxels [15]	0.030	0.067	0.026	0.038	0.028	0.057	0.015	0.134	0.050
TensoRF-CP [17]	0.041	0.107	0.059	0.052	0.036	0.069	0.033	0.194	0.074
TensoRF-VM [17]	0.022	0.073	0.022	0.030	0.018	0.058	0.014	0.138	0.047
CCNeRF-CP [18]	0.081	0.135	0.069	0.090	0.075	0.088	0.052	0.239	0.104
CCNeRF-HY [18]	0.035	0.105	0.054	0.055	0.038	0.080	0.031	0.189	0.073
Instant-NGP [20]	0.018	0.068	0.029	0.027	0.017	0.053	0.015	0.123	0.044
K-Planes-explicit [19]	0.020	0.057	0.028	0.027	0.019	0.051	0.010	0.132	0.043
K-Planes-hybrid [19]	0.019	0.058	0.029	0.026	0.019	0.051	0.012	0.123	0.042
NeRF [1]	0.041	0.087	0.035	0.044	0.046	0.060	0.022	0.184	0.065
Mip-NeRF [24]	0.040	0.085	0.030	0.043	0.041	0.057	0.020	0.177	0.062
Ours-S2	0.034	0.076	0.029	0.041	0.036	0.071	0.019	0.141	0.056
Ours-S4	0.022	0.066	0.022	0.034	0.022	0.061	0.013	0.127	0.046
Ours-S8	0.018	0.061	0.019	0.031	0.017	0.055	0.010	0.118	0.041
Ours-B2	0.024	0.073	0.024	0.036	0.025	0.064	0.016	0.127	0.049
Ours-B4	0.019	0.066	0.020	0.032	0.017	0.057	0.012	0.117	0.043
Ours-B8	0.016	0.063	0.018	0.028	0.015	0.051	0.009	0.112	0.039

Table 11: Quantitative results of storage size and reconstruction quality (PSNR) on each scene of the Synthetic-NSVF dataset. We highlight the **best score** and **second-best score**.

Method	<i>Bike</i>	<i>Lifestyle</i>	<i>Palace</i>	<i>Robot</i>	<i>Spaceship</i>	<i>Steamtrain</i>	<i>Toad</i>	<i>Wineholder</i>	Avg.
Size (MB)↓									
DVGO [11, 12]	4.0	4.1	4.7	4.0	4.9	4.3	4.2	4.0	4.3
Plenoxels [15]	6.1	8.1	10.0	5.8	6.2	6.5	11.1	6.6	7.6
TensoRF-CP [17]	22.2	21.5	21.8	18.5	29.3	22.9	24.7	19.0	22.5
TensoRF-VM [17]	18.6	15.1	18.5	13.5	23.7	18.3	19.2	14.3	17.6
CCNeRF-CP [18]	18.9	17.2	19.2	18.9	22.8	22.5	23.0	21.7	20.5
CCNeRF-HY [18]	18.9	17.2	19.2	18.9	22.8	22.5	23.0	21.7	20.5
Instant-NGP [20]	3.2	3.1	3.8	3.8	3.0	3.5	7.4	3.0	3.9
K-Planes-explicit [19]	40.7	43.6	42.2	41.5	41.2	41.6	41.5	42.5	41.9
K-Planes-hybrid [19]	40.2	43.2	41.9	41.9	41.2	41.8	41.2	42.7	41.8
NeRF [1]	4.6	4.6	4.6	4.6	4.6	4.6	4.6	4.6	4.6
Mip-NeRF [24]	2.3	2.3	2.3	2.3	2.3	2.3	2.3	2.3	2.3
Ours-S2	<b>0.5</b>	<b>0.5</b>	<b>0.5</b>	<b>0.5</b>	<b>0.5</b>	<b>0.5</b>	<b>0.5</b>	<b>0.5</b>	<b>0.5</b>
Ours-S4	<b>0.9</b>	<b>0.9</b>	<b>1.0</b>	<b>0.9</b>	<b>1.0</b>	<b>0.9</b>	<b>0.9</b>	<b>0.9</b>	<b>0.9</b>
Ours-S8	1.8	1.8	1.9	1.8	1.9	1.8	1.8	1.7	1.8
Ours-B2	1.5	1.5	1.5	1.5	1.5	1.4	1.5	1.4	1.5
Ours-B4	3.0	3.0	3.0	2.9	3.1	2.8	2.9	2.8	2.9
Ours-B8	5.9	6.0	6.1	5.8	6.1	5.7	5.8	5.7	5.9
PSNR↑									
DVGO [11, 12]	38.15	33.80	34.39	36.31	37.52	36.54	33.10	30.28	35.01
Plenoxels [15]	37.83	31.05	35.31	35.92	34.41	34.29	34.35	30.02	34.15
TensoRF-CP [17]	36.98	32.68	36.32	36.09	37.20	35.87	31.47	29.92	34.57
TensoRF-VM [17]	<b>39.45</b>	34.60	37.81	<b>38.57</b>	<b>38.76</b>	37.95	35.11	31.61	<b>36.73</b>
CCNeRF-CP [18]	34.96	30.59	32.93	32.79	33.96	34.03	28.86	27.80	31.99
CCNeRF-HY [18]	37.25	32.42	36.23	36.30	35.95	35.63	33.69	29.08	34.57
Instant-NGP [20]	37.98	27.50	37.09	37.04	27.12	29.05	<b>36.29</b>	32.02	33.01
K-Planes-explicit [19]	36.96	18.30	<b>37.91</b>	35.78	20.06	35.42	34.69	30.45	31.20
K-Planes-hybrid [19]	37.08	18.07	37.91	35.80	20.06	35.41	34.70	30.42	31.18
NeRF [1]	35.72	33.45	34.74	33.52	36.52	<b>40.89</b>	31.60	29.23	34.46
Mip-NeRF [24]	37.33	34.08	35.03	35.16	37.21	<b>41.59</b>	32.20	30.04	35.33
Ours-S2	37.12	33.84	35.29	35.37	36.93	35.77	32.18	31.12	34.70
Ours-S4	38.35	34.47	36.73	37.06	37.94	36.96	33.79	31.94	35.91
Ours-S8	39.14	<b>34.89</b>	37.80	38.16	38.48	<b>37.53</b>	35.09	<b>32.47</b>	36.69
Ours-B2	38.11	34.42	36.56	36.77	37.42	36.57	33.95	31.78	35.70
Ours-B4	38.92	34.83	37.66	37.96	38.19	37.30	35.29	32.45	36.58
Ours-B8	<b>39.39</b>	<b>35.16</b>	<b>38.46</b>	<b>38.52</b>	<b>38.56</b>	37.63	<b>36.22</b>	<b>32.77</b>	<b>37.09</b>

Table 12: Quantitative results of and reconstruction quality (SSIM, LPIPS) on each scene of the Synthetic-NSVF dataset. We highlight the **best score** and **second-best score**.

Method	<i>Bike</i>	<i>Lifestyle</i>	<i>Palace</i>	<i>Robot</i>	<i>Spaceship</i>	<i>Steamtrain</i>	<i>Toad</i>	<i>Wineholder</i>	Avg.
SSIM $\uparrow$									
DVGO [11, 12]	0.991	0.965	0.962	0.992	0.987	0.989	0.966	0.950	0.975
Plenoxels [15]	0.992	0.967	0.974	0.991	0.982	0.983	0.976	0.959	0.978
TensoRF-CP [17]	0.988	0.953	0.972	0.990	0.984	0.986	0.952	0.947	0.971
TensoRF-VM [17]	<b>0.993</b>	0.969	0.981	0.994	<b>0.988</b>	<b>0.991</b>	0.979	0.963	<b>0.982</b>
CCNeRF-CP [18]	0.980	0.936	0.938	0.978	0.973	0.975	0.904	0.920	0.950
CCNeRF-HY [18]	0.988	0.956	0.973	0.990	0.981	0.984	0.974	0.946	0.974
Instant-NGP [20]	0.986	0.955	0.976	0.990	0.966	0.976	<b>0.980</b>	0.959	0.973
K-Planes-explicit [19]	0.990	0.852	0.982	0.991	0.873	0.987	0.978	0.960	0.952
K-Planes-hybrid [19]	0.990	0.850	<b>0.982</b>	0.991	0.873	0.987	0.978	0.960	0.951
NeRF [1]	0.986	0.958	0.958	0.984	0.986	0.984	0.945	0.936	0.967
Mip-NeRF [24]	0.988	0.961	0.962	0.988	0.987	0.987	0.954	0.946	0.971
Ours-S2	0.988	0.960	0.964	0.989	0.984	0.984	0.958	0.955	0.973
Ours-S4	0.991	0.965	0.974	0.993	0.987	0.988	0.970	0.963	0.979
Ours-S8	0.992	0.968	0.979	0.994	0.988	0.990	0.978	<b>0.967</b>	0.982
Ours-B2	0.990	0.965	0.973	0.992	0.985	0.987	0.972	0.961	0.978
Ours-B4	0.992	0.968	0.979	0.994	0.987	0.989	0.979	0.966	0.982
Ours-B8	<b>0.992</b>	<b>0.970</b>	<b>0.983</b>	<b>0.994</b>	<b>0.988</b>	<b>0.990</b>	<b>0.983</b>	<b>0.969</b>	<b>0.984</b>
LPIPS $\downarrow$									
DVGO [11, 12]	0.011	0.053	0.043	0.013	0.020	0.018	0.045	0.055	0.032
Plenoxels [15]	0.011	0.047	0.026	0.013	0.025	0.028	0.031	0.046	0.028
TensoRF-CP [17]	0.022	0.080	0.029	0.016	0.028	0.031	0.065	0.080	0.044
TensoRF-VM [17]	0.010	0.046	0.020	0.010	0.020	0.017	0.028	0.047	0.025
CCNeRF-CP [18]	0.032	0.101	0.069	0.032	0.039	0.049	0.101	0.105	0.066
CCNeRF-HY [18]	0.020	0.073	0.029	0.015	0.031	0.031	0.037	0.075	0.039
Instant-NGP [20]	0.013	0.051	0.018	0.009	0.039	0.026	<b>0.020</b>	0.038	0.027
K-Planes-explicit [19]	0.011	0.223	0.021	0.012	0.175	0.017	0.027	0.041	0.066
K-Planes-hybrid [19]	0.012	0.219	0.022	0.012	0.177	0.016	0.027	0.041	0.066
NeRF [1]	0.021	0.067	0.045	0.023	0.023	0.031	0.066	0.075	0.044
Mip-NeRF [24]	0.019	0.063	0.041	0.018	0.022	0.027	0.059	0.066	0.039
Ours-S2	0.016	0.053	0.030	0.014	0.022	0.025	0.045	0.049	0.032
Ours-S4	0.012	0.045	0.020	0.008	0.018	0.017	0.031	0.040	0.024
Ours-S8	<b>0.010</b>	0.040	0.015	<b>0.007</b>	<b>0.016</b>	<b>0.014</b>	0.023	<b>0.035</b>	0.020
Ours-B2	0.013	0.044	0.020	0.010	0.021	0.020	0.029	0.043	0.025
Ours-B4	0.010	0.038	0.015	0.007	0.018	0.015	0.021	0.036	<b>0.020</b>
Ours-B8	<b>0.009</b>	<b>0.035</b>	<b>0.012</b>	<b>0.006</b>	<b>0.016</b>	<b>0.013</b>	<b>0.017</b>	<b>0.032</b>	<b>0.017</b>

Table 13: Quantitative results of storage size and reconstruction quality (PSNR) on each scene of the Tanks and Temples dataset. We highlight the **best score** and **second-best score**.

Method	<i>Barn</i>	<i>Caterpillar</i>	<i>Family</i>	<i>Ignatius</i>	<i>Truck</i>	Avg.
Size (MB)↓						
DVGO [11, 12]	9.2	7.6	6.3	5.5	7.3	7.2
Plenoxels [15]	14.7	10.7	9.3	8.5	12.3	11.1
TensoRF-CP [17]	37.7	33.0	28.5	31.8	33.8	33.0
TensoRF-VM [17]	29.1	26.6	23.7	23.4	28.5	26.3
CCNeRF-CP [18]	33.8	29.0	23.5	18.7	23.1	25.6
CCNeRF-HY [18]	33.8	29.0	23.5	18.7	23.1	25.6
Instant-NGP [20]	3.7	3.6	3.4	3.3	3.7	3.5
K-Planes-explicit [19]	40.2	39.8	35.9	37.3	39.2	38.5
K-Planes-hybrid [19]	43.7	42.3	38.3	39.7	41.5	41.1
NeRF [1]	4.6	4.6	4.6	4.6	4.6	4.6
Mip-NeRF [24]	2.3	2.3	2.3	2.3	2.3	2.3
Ours-S2	0.5	0.5	0.5	0.5	0.5	0.5
Ours-S4	1.0	1.0	0.9	1.0	1.0	1.0
Ours-S8	1.9	1.9	1.8	1.9	1.8	1.9
Ours-B2	1.6	1.6	1.5	1.6	1.6	1.6
Ours-B4	3.1	3.1	2.9	3.2	3.1	3.1
Ours-B8	6.1	6.0	5.8	6.3	6.0	6.0
PSNR↑						
DVGO [11, 12]	26.94	25.76	33.73	28.23	27.14	28.36
Plenoxels [15]	24.50	25.27	30.01	27.87	26.69	26.87
TensoRF-CP [17]	27.03	25.27	32.78	28.27	26.30	27.93
TensoRF-VM [17]	27.50	26.30	34.16	28.38	26.92	28.65
CCNeRF-CP [18]	25.19	23.41	30.59	27.09	24.95	26.25
CCNeRF-HY [18]	26.41	24.78	32.75	27.81	26.37	27.62
Instant-NGP [20]	26.10	25.76	32.48	26.80	27.46	27.72
K-Planes-explicit [19]	27.39	25.37	33.38	26.99	26.94	28.01
K-Planes-hybrid [19]	27.32	25.52	33.39	26.98	26.84	28.01
NeRF [1]	27.27	25.32	31.56	27.29	26.47	27.58
Mip-NeRF [24]	27.45	25.41	32.38	27.57	26.05	27.77
Ours-S2	27.35	25.70	33.38	27.83	26.96	28.24
Ours-S4	27.61	25.86	33.90	27.82	27.29	28.50
Ours-S8	27.69	25.95	34.33	27.93	27.47	28.67
Ours-B2	27.65	25.87	33.86	27.78	27.31	28.49
Ours-B4	27.74	25.97	34.33	27.92	27.46	28.68
Ours-B8	27.69	26.00	34.45	27.92	27.54	28.72

Table 14: Quantitative results of reconstruction quality (SSIM, LPIPS) on each scene of the Tanks and Temples dataset. We highlight the **best score** and **second-best score**.

Method	<i>Barn</i>	<i>Caterpillar</i>	<i>Family</i>	<i>Ignatius</i>	<i>Truck</i>	Avg.
SSIM $\uparrow$						
DVGO [11, 12]	0.839	0.905	0.962	0.943	0.906	0.911
Plenoxels [15]	0.842	0.905	0.959	0.942	0.910	0.912
TensoRF-CP [17]	0.845	0.884	0.951	0.939	0.887	0.901
TensoRF-VM [17]	0.866	0.913	0.967	0.949	0.913	0.922
CCNeRF-CP [18]	0.794	0.859	0.931	0.924	0.858	0.873
CCNeRF-HY [18]	0.828	0.887	0.957	0.938	0.895	0.901
Instant-NGP [20]	0.862	0.920	0.968	0.953	0.929	0.926
K-Planes-explicit [19]	0.876	0.909	0.963	0.938	0.917	0.921
K-Planes-hybrid [19]	0.872	0.912	0.963	0.940	0.917	0.921
NeRF [1]	0.845	0.893	0.943	0.935	0.893	0.902
Mip-NeRF [24]	0.846	0.888	0.947	0.933	0.890	0.901
Ours-S2	0.853	0.898	0.956	0.941	0.897	0.909
Ours-S4	0.864	0.904	0.962	0.944	0.908	0.916
Ours-S8	0.872	0.907	0.965	0.945	0.913	0.920
Ours-B2	0.869	0.904	0.963	0.944	0.907	0.917
Ours-B4	0.877	0.909	0.966	0.946	0.914	0.922
Ours-B8	0.882	0.910	0.968	0.947	0.917	0.925
LPIPS $\downarrow$						
DVGO [11, 12]	0.291	0.168	0.070	0.086	0.159	0.155
Plenoxels [15]	0.276	0.162	0.076	0.094	0.151	0.152
TensoRF-CP [17]	0.275	0.212	0.081	0.092	0.199	0.172
TensoRF-VM [17]	0.248	0.157	0.059	0.077	0.147	0.138
CCNeRF-CP [18]	0.371	0.263	0.108	0.117	0.237	0.219
CCNeRF-HY [18]	0.306	0.214	0.076	0.100	0.184	0.176
Instant-NGP [20]	0.210	0.118	0.040	0.056	0.106	0.106
K-Planes-explicit [19]	0.196	0.138	0.065	0.107	0.126	0.126
K-Planes-hybrid [19]	0.199	0.133	0.059	0.103	0.125	0.124
NeRF [1]	0.282	0.189	0.100	0.098	0.185	0.171
Mip-NeRF [24]	0.281	0.194	0.093	0.101	0.184	0.171
Ours-S2	0.220	0.154	0.062	0.079	0.153	0.134
Ours-S4	0.204	0.145	0.054	0.075	0.138	0.123
Ours-S8	0.192	0.138	0.048	0.074	0.128	0.116
Ours-B2	0.198	0.144	0.052	0.075	0.139	0.122
Ours-B4	0.187	0.136	0.046	0.072	0.128	0.114
Ours-B8	0.180	0.133	0.043	0.072	0.121	0.109